

Nonlinear Spectral Unmixing using Bézier Surfaces

Bikram Koirala, *Member, IEEE*, Behnood Rasti, *Senior Member, IEEE*, Zakaria Bnoukacem,
Paul Scheunders, *Senior Member, IEEE*

Abstract—Accurate estimation of the fractional abundances of intimately mixed materials from spectral reflectances is generally hard due to a highly nonlinear relationship between the measured spectrum and the composition of the material. Changes in the acquisition and the illumination conditions cause variability in the spectral reflectance, further complicating the spectral unmixing procedure. In this work, we propose a methodology for unmixing intimate mixtures that can tackle both nonlinearity and spectral variability. A supervised approach is proposed that characterizes the nonlinear data manifolds by high-dimensional Bézier surfaces. To deal with spectral variability, a manifold transformation procedure is designed.

To generate Bézier surfaces, training samples are required that are uniformly distributed throughout the data manifold. For this, we recently generated a hyperspectral dataset of intimate mineral powder mixtures by homogeneously mixing five different clay powders (Kaolin, Roof clay, Red clay, mixed clay, and Calcium hydroxide) in laboratory settings. In total 330 samples (325 mixtures and five pure materials) were prepared. The ground fractional abundances of these mixtures uniformly cover the five-dimensional probability simplex. The spectral reflectances of these samples were acquired by multiple sensors with a large variation in sensor types, platforms, and acquisition conditions. Experiments are conducted both on simulated and real intimate mineral powder mixtures. Comparison with a number of unsupervised unmixing methods demonstrates the potential of the proposed approach.

Index Terms—Hyperspectral, spectral variability, nonlinearity, mixing models, mineral powder mixtures, Bézier surface

I. INTRODUCTION

Hyperspectral unmixing aims to estimate the fractional contributions (abundances) of spectra of pure materials (endmembers) within a pixel’s field of view. This is generally achieved by minimizing the error between the observed spectral reflectance and the spectrum generated by a specific mixing model. In the remote sensing community, the linear mixing model (LMM) [1] is the most popular mixing model. This model assumes that every incident light ray interacts with a single, pure material within the pixel’s instantaneous field of view before it reaches the sensor. To account for the physical constraints of non-negativity and the sum-to-one requirement for fractional abundances, the Fully Constrained Least Squares Unmixing procedure (FCLSU) was introduced [2], [3]. The LMM demonstrates excellent performance in situations characterized by extensive flat regions on the Earth’s surface, with well-defined and separate areas containing distinct endmembers.

Bikram Koirala (corresponding author), Zakaria Bnoukacem, and Paul Scheunders are with Imec-Visionlab, Department of Physics, University of Antwerp (CDE) Universiteitsplein 1, B-2610 Antwerp, Belgium; Bikram.Koirala@uantwerpen.be; paul.scheunders@uantwerpen.be

Behnood Rasti is with Faculty of Electrical Engineering and Computer Science, Technische Universität Berlin, Berlin, Germany; behnood.rasti@gmail.com

Deep learning has significantly transformed linear unmixing through the widespread use of deep autoencoder architectures. In these structures, the input consists of reflectance spectra, and the output consists of reconstructed spectra. The encoder is responsible for converting the input spectra into fractional abundances, and subsequently, the decoder transforms these abundances back into reconstructed spectra through linear layers, with the endmembers serving as the weights. In [4], autoencoders applied to hyperspectral unmixing are categorized into five distinct groups: (a) Sparse nonnegative autoencoders [5]; (b) Variational autoencoders [6], [7]; (c) Adversarial autoencoders [8], [9]; (d) Denoising autoencoders [10]; (e) Convolutional autoencoders [11], [12]. In [13], unmixing using deep image prior [13] was proposed for linear unmixing. In [14], a convolutional autoencoder is combined with a transformer. In [15], a powerful linear unmixing approach was proposed that integrates the spatial correlation among neighboring pixels with the geometric characteristics of the linear simplex.

However, the effectiveness of the LMM diminishes in scenarios when hyperspectral images are acquired from the Earth’s surface featuring complex geometric structures. In such cases, incident light rays may interact with multiple pure materials within a pixel before reaching the sensor. Consequently, the acquired reflectance spectra become highly nonlinear combinations of the reflectances of the individual endmembers. To tackle this challenge, nonlinear unmixing models have been developed [16].

A widely explored category of nonlinear unmixing models is the category of bilinear models. These models assume that the incident light interacts with a maximum of two pure materials before reaching the sensor, introducing an additional mixing term in the linear model through the Hadamard product between the endmembers. The Fan model [17] is a variant of this approach. The major limitation of this model is that it does not perform well on linearly mixed datasets. To overcome this limitation, extensions such as the polynomial post-nonlinear mixing model (PPNM) [18], the generalized bilinear model (GBM) [19], and the linear-quadratic model (LQM) [20] have been introduced. These models incorporate hyperparameters to characterize the balance between linear and nonlinear terms. To capture higher-order interactions of incident light before reaching the sensor, various nonlinear mixing models have been developed, including the multilinear mixing model (MLM) [21], the p-linear ($p > 2$) mixture model (pLMM) [22], [23], [24], etc.). The approach presented in [25] transforms the task of solving bilinear mixing models into a linear one by exploiting the geometric characteristics of bilinear mixing models. The most advanced nonlinear mixing models include physics-based radiative transfer models, fre-

quently utilized for modeling spectral reflectances of intimate mixtures. These models conceptualize the medium as a half-space filled with particles characterized by known densities and distributions of physical attributes. In the remote sensing community, the Hapke model is the most popular one. It was specifically crafted to explain the interaction between light and intimately mixed materials [26], [27]. This model predicts the areal fractions of materials within the mixture by converting reflectance spectra into their single-scattering albedos and then applying linear unmixing.

Although regularly applied in linear unmixing, a limited number of studies explored the potential of deep autoencoder architectures for nonlinear unmixing. The majority of deep learning-based nonlinear unmixing methods are built upon autoencoder architectures grounded in PPNM [28], [29]. A nonlinear low-rank tensor unmixing algorithm was introduced in [30] to solve the generalized bilinear model. In [31], an autoencoder network based on MLM was proposed for unsupervised hyperspectral unmixing. In [32], a dual-stream network was proposed to solve an extended multilinear mixing model.

In [33], the inherent nonlinearity in the data was modeled via deep autoencoder networks. Recently, in [34], a nonlinear unmixing approach was proposed employing the Hapke model in conjunction with convolutional neural networks.

Efforts to comprehend the nonlinearity within a mixture have been made through the application of supervised machine learning techniques [35], [36], [37], [38]. For instance, in [37], [38], a mapping between measured spectra and linearly mixed spectra was learned by employing training samples and a supervised regression algorithm. Subsequently, the FCLSU procedure is implemented to deduce the fractional abundances from mapped spectra of test samples. However, a significant drawback of such supervised approaches is their limited generalizability [39]. These models may not perform well on test samples that lie on different data manifolds from the training set. This often occurs due to variability in measured spectra due to variations in illumination conditions, distance, and orientation from the sensor and is often described as external spectral/endmember variability [40][39]. These effects often cause a (global or pixel-based) scaling of the spectral reflectance. Additional forms of external variability may arise across various datasets, such as those acquired from different sensors or when different white calibration panels are used. These factors result in a wavelength-dependent variation in the measured spectra.

Various algorithms address external spectral/endmember variability. These algorithms can be categorized into two groups: methods based on endmember bundles and those employing physical and statistical models ([41], [42], [43]). The first category of algorithms establishes a collection of multiple spectral signatures (endmember bundles) to characterize each endmember class ([44]). These endmember bundles can be derived from the hyperspectral image through the implementation of endmember bundle extraction methods ([45], [46], [47]). As indicated in [48], endmember bundles do not fully represent all variations among endmembers in hyperspectral images. The second category of algorithms addresses spectral

variability by either incorporating additional variability terms in the linear mixing model ([49], [50], [51]) or relying on a statistical representation of the endmembers ([52], [53], [54]). In [55], an algorithm is devised to bridge the gap between endmember bundle-based methods and parametric physics-based models. Meanwhile, in [56], spectral variability was addressed as a denoising problem.

There is scarce research in the literature specifically dedicated to addressing spectral variability in the context of nonlinear unmixing. In [57], [58], bilinear models were extended by incorporating a scaling term to address external spectral variability. In [59], a band-wise scaling of the LMM is suggested to account for either spectral variability in the linear case or to perform nonlinear mixing. In [60], endmembers were modeled by a normal distribution to mitigate the impact of endmember variability in bilinear models. In [61], an approach called neighbor-band ratio unmixing (NBRU) was introduced for estimating fractional abundances from mineral mixtures, and its robustness against endmember variability was verified.

In general, the inversion of a model that simultaneously addresses spectral variability and nonlinearity tends to be non-convex. Most of the proposed models have large amounts of hyperparameters, posing challenges for accurate abundance estimation. Additionally, depending on a single model makes a method inflexible, especially in cross-sensor scenarios. In [39], it was demonstrated that the nonlinearity of a dataset undergoes changes by data manipulation only when the curvature of the manifold is altered. However, existing nonlinear mixing models lack scaling invariance because the spectral reflectance is a nonlinear function of both the endmembers and fractional abundances. The nonlinearity of a dataset undergoes changes due to intrinsic spectral/endmember variability. This phenomenon commonly arises when there are changes in the chemical or geometric properties, such as variations in grain size distributions of the materials.

To tackle both nonlinearity and external spectral variability, we recently developed a robust supervised unmixing method tailored for the nonlinear hyperspectral unmixing of binary intimate mixtures [39]. This method utilizes the geodesic distance between endmembers and binary mixed spectra as a representation that is invariant to variations in sensor type. To tackle scaling effects due to the variation in illumination conditions, distance, and orientation from the sensor, the representation was obtained in the unit hypersphere. The success of this method suggests that external variability does not change the intrinsic nonlinearity of the dataset, although the spectral reflectance of the same sample acquired by two different sensors lies on two different data manifolds.

For data manifolds generated by mixtures of more than two pure materials, an accurate determination of geodesic distances is infeasible. This limits the extension of our method [39] to higher dimensional data manifolds (where the number of pure materials exceeds 2). To tackle this challenge, in this study, we utilized the properties of Bézier surfaces to reconstruct higher dimensional nonlinear data manifolds. Reconstruction of a Bézier surface requires training samples represented as control points (spectral reflectances). The process of estimating the

fractional abundances of test samples involves minimizing the reconstruction error between the input spectrum and the Bézier surface. To address spectral variability caused by variation in sensor type, we learn a transformation function between the training and test data manifolds by leveraging the spectral reflectance of the pure materials (endmembers). We should note that the proposed method cannot tackle intrinsic spectral variability.

A. Contributions and Novelties

The contribution of the proposed method is five fold.

- 1) Generalization by characterizing any nonlinear data manifold: Unlike existing mixing models that are valid only for a specific type of mixing scenario, the proposed method utilized the spectral reflectances of control points to reconstruct the data manifold. This leads to a generalized model that can cope with various nonlinear mixing scenarios.
- 2) Tackling spectral variability: The proposed method not only characterizes the nonlinearity of the dataset but also tackles the spectral variability caused by variation in sensor type. Except for the methodology proposed in [39], none of the state-of-the-art methods can accurately perform both tasks together.
- 3) Tackling scaling effects of mixtures: In [39], the random scaling effects were tackled by projecting the dataset onto the unit hypersphere. This is in itself however a nonlinear transformation. Such a nonlinear transformation affects the original mixing model assumption. To overcome this issue, random scaling effects of mixed spectra are tackled in the reflectance space by utilizing the spectral reflectance of endmembers acquired at the same acquisition conditions.
- 4) Reconstruction of spectral reflectance of test samples: Unlike the methodology proposed in [39], this method not only estimates the fractional abundances of test samples but can also accurately reconstruct their spectral reflectance.

The rest of the paper is structured as follows: Section II is dedicated to prior work. We present some popular mixing models and the supervised geodesic unmixing approach. Section III provides a detailed explanation of the proposed methodology. In Section IV, we describe the simulated dataset and real intimate mineral powder mixtures on which our methodology is validated. In Section V, we outline the experiments and present the results, followed by a discussion in Section VI. The conclusion of this work is presented in Section VII.

II. RELEVANT PRIOR WORK

A. Hyperspectral mixing models

The spectral reflectances of the hyperspectral dataset $\mathbf{Y}(\{\mathbf{y}_i\}_{i=1}^N \in \mathbf{R}_+^d)$ composed of d spectral bands and N samples can be modeled as:

$$\mathbf{y}_i = F(\mathbf{E}, \mathbf{a}_i) + \boldsymbol{\eta}_i, \quad (1)$$

with p endmembers $\mathbf{E}(\{\mathbf{e}_j\}_{j=1}^p \in \mathbf{R}_+^d)$ and their fractional abundances $\mathbf{A}(\{\mathbf{a}_i\}_{i=1}^N \in \mathbf{R}_+^p)$, F is a nonlinear function and $\boldsymbol{\eta}_i$ represents Gaussian noise. By shaping function F , any mixing model can be derived.

1) *Linear mixing model*: The linear mixing model reconstructs the input spectrum by linearly combining endmembers and the fractional abundances:

$$\mathbf{y}_i = \mathbf{E}\mathbf{a}_i + \boldsymbol{\eta}_i, \quad (2)$$

When the non-negative and sum-to-one constraints are considered, the FCLSU estimates the fractional abundances by minimizing $\|\mathbf{y}_i - \mathbf{E}\mathbf{a}_i\|^2$ s.t. $\sum_j a_{ji} = 1, \forall j : a_{ji} \geq 0$.

2) *Bilinear mixing models*: Bilinear mixing models have been designed to explain secondary reflections of the incident light before reaching the sensor. In [17], the Fan model is derived through the first-order Taylor series expansion of a general nonlinear mixing function:

$$\begin{aligned} \mathbf{y}_i &= F(\mathbf{E}\mathbf{a}_i) + \boldsymbol{\eta}_i \\ &= \mathbf{E}\mathbf{a}_i + \sum_{j=1}^{p-1} \sum_{k=j+1}^p a_{ji}a_{ki}\mathbf{e}_j \odot \mathbf{e}_k + \boldsymbol{\eta}_i \end{aligned} \quad (3)$$

where \odot is the elementwise multiplication of two vectors. As we already mentioned in the introduction section, the primary disadvantage of the Fan model is its limited performance when applied to linearly mixed data. GBM [19], PPNM [18], and LQM [20] are developed to generalize the bilinear mixing model to the linear case. We like to clarify that these models are mathematical models and allow spectrum reflectances of materials to have values outside of the physical range [0,1].

3) *Multilinear mixing models*: To consider higher-order reflections of the incident light before reaching the sensor, MLM [21] and the p-linear ($p > 2$) mixture model [22], [23], [24] have been proposed.

4) *Hapke model*: The Hapke model [26], [27] is designed to describe the optical properties of intimately mixed mineral powders. In the context of intimate mixtures, the incident light undergoes multiple interactions with particles before reaching the sensor. The major assumption of the Hapke model is that the particles are significantly larger than the wavelength of light, are spherical, and scatter light isotropically. In general, this model assumes that information regarding the physical characteristics of the material (such as particle size and surface roughness) and the real and imaginary parts of the optical indexes are known a priori. In [62], this model was simplified for remote sensing applications. This simplified version of the Hapke model establishes a relationship between the bidirectional reflectance \mathbf{y}_i and the single scattering albedos (SSA) $\mathbf{w}_i \in \mathbf{R}_+^d$ through the following equation:

$$\begin{aligned} \mathbf{y}_i &= F(\mathbf{E}, \mathbf{a}_i) + \boldsymbol{\eta}_i \\ &= \frac{\mathbf{w}_i}{(1 + 2\mu\sqrt{1 - \mathbf{w}_i})(1 + 2\mu_0\sqrt{1 - \mathbf{w}_i})} + \boldsymbol{\eta}_i \\ &= \frac{\mathbf{W}\mathbf{E}\mathbf{a}_i}{(1 + 2\mu\sqrt{1 - \mathbf{W}\mathbf{E}\mathbf{a}_i})(1 + 2\mu_0\sqrt{1 - \mathbf{W}\mathbf{E}\mathbf{a}_i})} + \boldsymbol{\eta}_i \end{aligned} \quad (4)$$

where $\mu = \cos(\theta_e)$ and $\mu_0 = \cos(\theta_i)$ represent the cosines of the angles with the normal of the outgoing and incoming

radiation, respectively and $\mathbf{W}^E(\{\mathbf{w}_j^E\}_{j=1}^p \in \mathbf{R}_+^d)$ represents the SSA of endmembers. The SSA of a material is the ratio of photons scattered by the material to the total number of photons affected by that material:

$$\mathbf{w}_j^E = \frac{\mathbf{s}_j}{\mathbf{s}_j + \mathbf{a}_j} \quad (5)$$

where \mathbf{s}_j and \mathbf{a}_j are the scattering and absorption spectra of the material.

B. Supervised geodesic unmixing

In [63], a distance geometric framework for nonlinear hyperspectral unmixing was developed. A commonly used data-driven approach for approximating geodesic distances on a manifold involves constructing a nearest-neighbor graph on the data. The geodesic distance between any two points is then defined as the shortest path distance along the graph. We have demonstrated in [39] that when the curvature of the manifold is non-constant, the relationship between the geodesic distance and the fractional abundance is nonlinear. To tackle this challenge, we have developed a robust supervised geodesic unmixing approach that can accurately estimate the fractional abundances of binary mixtures by combining spectral mixture modeling with a supervised nonlinear regression approach [39], [64].

III. NONLINEAR UNMIXING USING A BÉZIER SURFACE

A. Hyperspectral data modeling using a Bézier surface

Existing nonlinear mixing models either oversimplify the intricate interaction between the incident light and material or, by considering various interactions, inherently become complex and non-invertible. Furthermore, the parameters of nonlinear mixing models (e.g., bilinear models) are typically challenging to interpret and to relate to the actual fractional abundances. On the other hand, supervised machine-learning algorithms proposed in [36], [37], [38] have limited generalizability. Although the supervised geodesic unmixing approach of [39] tackles these challenges, it is limited to binary mixtures.

To extend the methodology proposed in [39] to higher order mixtures, in this work, we will utilize the properties of higher dimensional Bézier surfaces. A Bézier surface is a nonlinear surface that can be reconstructed by the interpolation of a set of control points (reflectance spectra). A general n^{th} order Bézier surface has $\frac{(n+p-1)!}{n!(p-1)!}$ control points $\mathbf{C}_{i_1, \dots, i_p}$, where p denotes the number of endmembers, and $\sum i_k = n, i_k \geq 0$:

$$\mathbf{y} = F(\mathbf{E}, \mathbf{a}) = \sum_{i_1} \cdots \sum_{i_p} \frac{n!}{\prod_{k=1}^p i_k!} \left(\prod_{k=1}^p a_k^{i_k} \right) \mathbf{C}_{i_1, \dots, i_p} \quad (6)$$

As an example, take ternary mixtures, for which the Bézier surface is defined as:

$$\mathbf{y} = F(\mathbf{E}, \mathbf{a}) = \sum_i \sum_j \sum_k \frac{n!}{i!j!k!} a_1^i a_2^j a_3^k \mathbf{C}_{i,j,k} \quad (7)$$

where $i + j + k = n, i, j, k \geq 0$. \mathbf{y} is the reconstructed spectrum of a mixture with fractional abundances given by

$\mathbf{a} = [a_1, a_2, a_3]^T$. The fractional abundances obey both the non-negativity and the sum-to-one constraint. The higher the value of n , the better the reconstruction.

To further enhance clarity, we show a nonlinear data manifold in Fig.1(a). As can be observed, there are 36 control points (blue circles) to fit a 7th-order Bézier surface. Among them, three control points are endmembers ($\mathbf{C}_{7,0,0}$, $\mathbf{C}_{0,7,0}$ and $\mathbf{C}_{0,0,7}$). The indices can be used to determine the ground truth fractional abundance of a control point. For example, the fractional abundance of the control point $\mathbf{C}_{2,2,3}$ is calculated as $[i/n, j/n, k/n]^T = [2/7, 2/7, 3/7]^T$. Endmembers are defined by having only one non-zero index, whereas binary mixtures are characterized by having only two non-zero indices. For instance, binary mixtures include $\mathbf{C}_{0,4,3}$, $\mathbf{C}_{2,5,0}$, $\mathbf{C}_{2,0,5}$ and so forth. In Fig. 1 (b), we depict the fractional abundances of the control points of a Bézier surface of order $n = 7$. As depicted, the fractional abundances of the control points uniformly span the probability simplex.

Estimating the fractional abundances of any test spectrum then boils down to minimization of the reconstruction error between the input spectrum (\mathbf{y}) and the spectrum generated by applying Eq. (7):

$$\hat{\mathbf{a}} = \arg \min_{\mathbf{a}} \left\| \mathbf{y} - \sum_i \sum_j \sum_k \frac{n!}{i!j!k!} a_1^i a_2^j a_3^k \mathbf{C}_{i,j,k} \right\|^2 \quad (8)$$

$$\text{s.t. : } \sum_{l=1}^p a_l = 1, \forall l : a_l \geq 0$$

In this study, we aim to minimize Eq. (8) using the optimization toolbox `fmincon`, which is designed for finding the minimum of a constrained nonlinear multivariable function. The optimization process will employ the sequential quadratic programming algorithm.

We like to clarify that, the proposed method can be easily generalized to mixtures with $p > 3$. Note that the proposed approach not only allows estimating the fractional abundances from the spectral reflectance of an unknown mixture using Eq. (8), but is also capable of reconstructing the spectral reflectance of a mixture of known composition, using Eq. (7).

1) *Approximating linearly mixed datasets using a Bézier surface:* When the order of the Bézier surface is $n = 1$, the Bézier surface boils down to the linear simplex. For ternary mixtures:

$$\begin{aligned} \mathbf{y} &= \sum_i \sum_j \sum_k \frac{1!}{i!j!k!} a_1^i a_2^j a_3^k \mathbf{C}_{i,j,k} \\ &= a_1^1 a_2^0 a_3^0 \mathbf{C}_{1,0,0} + a_1^0 a_2^1 a_3^0 \mathbf{C}_{0,1,0} + a_1^0 a_2^0 a_3^1 \mathbf{C}_{0,0,1} \\ &= [\mathbf{C}_{1,0,0}, \mathbf{C}_{0,1,0}, \mathbf{C}_{0,0,1}] [a_1, a_2, a_3]^T \end{aligned} \quad (9)$$

where $\mathbf{C}_{1,0,0}$, $\mathbf{C}_{0,1,0}$, and $\mathbf{C}_{0,0,1}$ denote endmember 1, endmember 2, and endmember 3, respectively.

2) *Approximating bilinearly mixed datasets using a Bézier surface:* When the order of the Bézier surface is $n \geq 2$, the

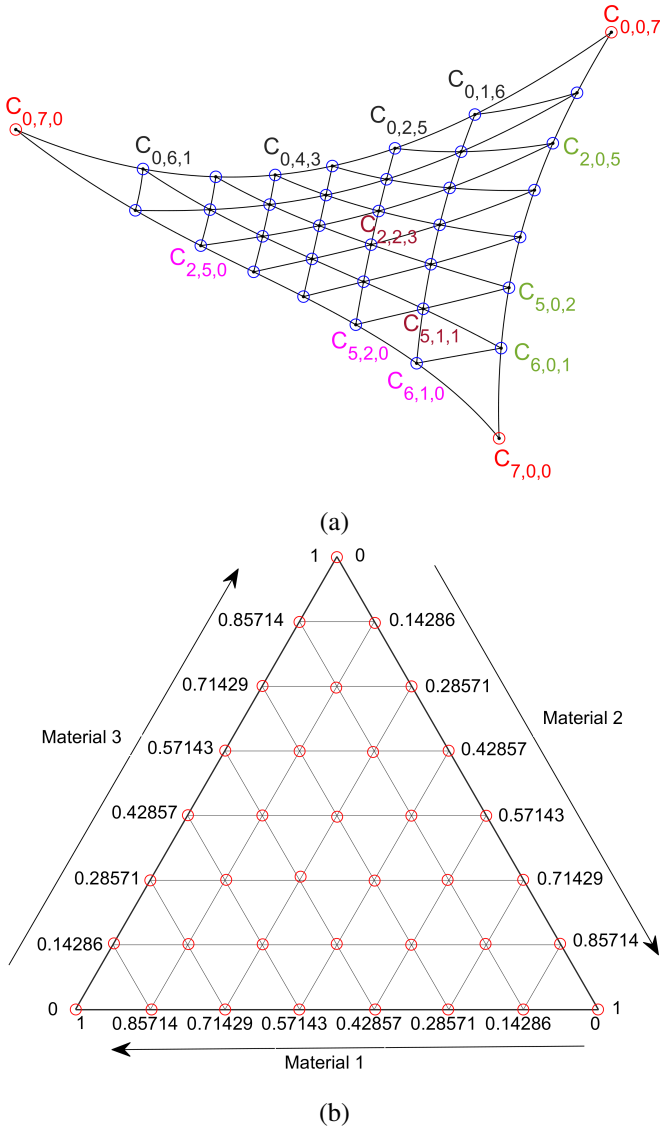


Fig. 1: (a) Nonlinear data manifold, represented by a 7th-order Bézier surface. Labels for some specific control points have been incorporated; (b) The ternary diagram of three material mixtures.

Bézier surface can approximate bilinearly mixed datasets. For ternary mixtures, in the case of order $n = 2$, one obtains:

$$\begin{aligned}
 \mathbf{y} &= \sum_i \sum_j \sum_k \frac{2!}{i!j!k!} a_1^i a_2^j a_3^k \mathbf{C}_{i,j,k} \\
 &= a_1^2 a_2^0 a_3^0 \mathbf{C}_{2,0,0} + 2a_1^1 a_2^1 a_3^0 \mathbf{C}_{1,1,0} + 2a_1^1 a_2^0 a_3^1 \mathbf{C}_{1,0,1} + \\
 &+ a_1^0 a_2^2 a_3^0 \mathbf{C}_{0,2,0} + 2a_1^0 a_2^1 a_3^1 \mathbf{C}_{0,1,1} + a_1^0 a_2^0 a_3^2 \mathbf{C}_{0,0,2} \\
 &= [\mathbf{C}_{2,0,0}, \mathbf{C}_{0,2,0}, \mathbf{C}_{0,0,2}] [a_1^2, a_2^2, a_3^2]^T + 2a_1 a_2 \mathbf{C}_{1,1,0} + \\
 &+ 2a_1 a_3 \mathbf{C}_{1,0,1} + 2a_2 a_3 \mathbf{C}_{0,1,1}
 \end{aligned} \quad (10)$$

where $\mathbf{C}_{2,0,0}$, $\mathbf{C}_{0,2,0}$, and $\mathbf{C}_{0,0,2}$ denote endmember 1, endmember 2, and endmember 3, respectively. $\mathbf{C}_{1,1,0}$, $\mathbf{C}_{1,0,1}$, and $\mathbf{C}_{0,1,1}$ describe a bilinear mixture of endmember 1 and endmember 2, endmember 1 and endmember 3, and endmember 2 and endmember 3, respectively. The ground truth fractional abundances of these three control points are respectively

$[0.5, 0.5, 0]^T$, $[0.5, 0, 0.5]^T$, and $[0, 0.5, 0.5]^T$. When control points in itself are generated by the linear mixing model, this bilinear model again boils down to the linear mixing model:

$$\begin{aligned}
 \mathbf{y} &= [\mathbf{C}_{2,0,0}, \mathbf{C}_{0,2,0}, \mathbf{C}_{0,0,2}] [a_1^2, a_2^2, a_3^2]^T + 2a_1 a_2 (0.5 \mathbf{C}_{2,0,0} + \\
 &+ 0.5 \mathbf{C}_{0,2,0}) + 2a_1 a_3 (0.5 \mathbf{C}_{2,0,0} + 0.5 \mathbf{C}_{0,0,2}) + \\
 &+ 2a_2 a_3 (0.5 \mathbf{C}_{0,2,0} + 0.5 \mathbf{C}_{0,0,2}) \\
 &= (a_1^2 + a_1 a_2 + a_1 a_3) \mathbf{C}_{2,0,0} + (a_2^2 + a_1 a_2 + a_2 a_3) \mathbf{C}_{0,2,0} \\
 &+ (a_3^2 + a_1 a_3 + a_2 a_3) \mathbf{C}_{0,0,2} \\
 &= (a_1^2 + a_1 a_2 + a_1 (1 - a_1 - a_2)) \mathbf{C}_{2,0,0} + (a_2^2 + a_1 a_2 + \\
 &+ a_2 (1 - a_1 - a_2)) \mathbf{C}_{0,2,0} + (a_3^2 + a_1 a_3 + (1 - a_1 - a_3) a_3) \\
 &\mathbf{C}_{0,0,2} \\
 &= [\mathbf{C}_{2,0,0}, \mathbf{C}_{0,2,0}, \mathbf{C}_{0,0,2}] [a_1, a_2, a_3]^T
 \end{aligned} \quad (11)$$

3) *Approximating a complex data manifold using a Bézier surface:* When the nonlinearity of the dataset is complex, a Bézier surface of higher order is required. One such example is a dataset generated by the Hapke model. To demonstrate that the proposed method indeed can characterize nonlinear surfaces generated by the Hapke model, in Fig. 2, we show the PCA-reduced original and reconstructed data manifolds. To generate this manifold, three endmem-

bers; $\begin{pmatrix} 0.6 & 0.2 & 0.2 \\ 0.2 & 0.6 & 0.2 \\ 0.2 & 0.2 & 0.6 \end{pmatrix}$ were mixed nonlinearly using

the Hapke model. The fractional abundances were generated uniformly (see Fig. 1) to reconstruct a Bézier surface of order 7. As can be observed, the reconstructed data points (using the ground truth fractional abundances) almost overlap with the true data points. Since the method attempts to generate a smooth surface, small deviations in the positions of the control points (except for the endmembers) occur.

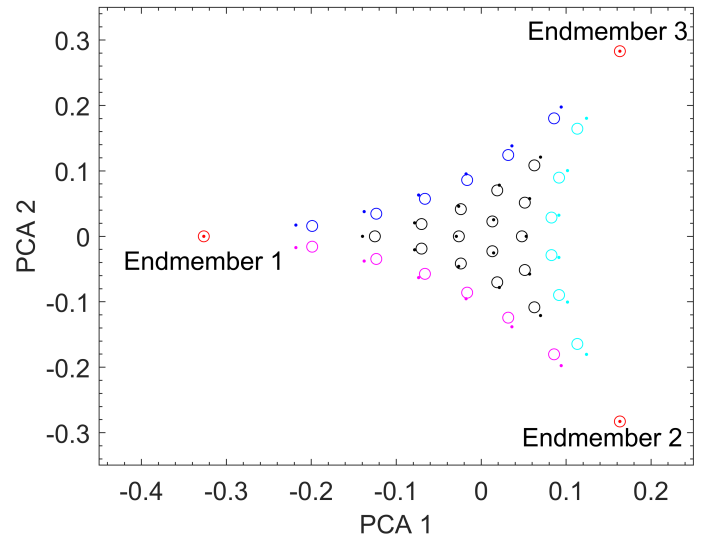


Fig. 2: The PCA-reduced data manifolds generated by the Hapke model. Magenta, blue, and cyan circles denote binary mixtures, while the black circles denote ternary mixtures. Reconstructed data points are denoted with dots.

B. Tackling spectral variability

Although the proposed approach can accurately characterize the nonlinearity of a hyperspectral dataset, it is susceptible to spectral variability induced by variations in illumination conditions and acquisition conditions.

1) *Tackling random scaling effects*: We first treat the situation in which identical acquisition conditions are applied for all mixtures. This is the situation where a single sensor is applied, and the calibration procedure, illumination conditions, and illumination and viewing angles do not change when acquiring spectra from all mixtures.

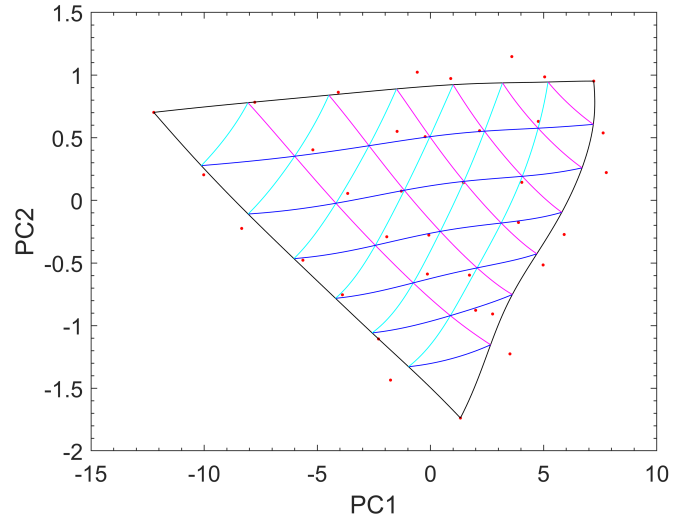
In that scenario, the measured bidirectional reflectance may suffer from random scaling effects, due to variations in scattering properties of mixtures with varying composition. In Fig. 3(a), we show the PCA reduced data manifold of the ternary mixtures of Kaolin, Red clay, and $\text{Ca}(\text{OH})_2$ acquired by an ASD spectroradiometer (see [65] for detailed information). Even though the ground truth fractional abundances of these mixtures uniformly cover the probability simplex (see Fig. 1), it is not reflected in the data manifold (see Fig. 3(a)) due to random scaling effects in the measured bidirectional reflectance.

One approach to address this challenge is to acquire hemispherical reflectance instead of the bidirectional reflectance that is measured in remote sensing applications. This is however limited to laboratory settings by using an integrating sphere. In [39], random scaling effects were tackled, by projecting all data points onto the unit hypersphere (i.e., dividing the spectra by their length). Although this approach worked well for binary mixtures, for higher order mixtures it can reduce the intrinsic dimensionality of the dataset if the spectral angles between the endmembers are low. In this way, mixtures of three pure materials may be projected onto the curve connecting two endmembers.

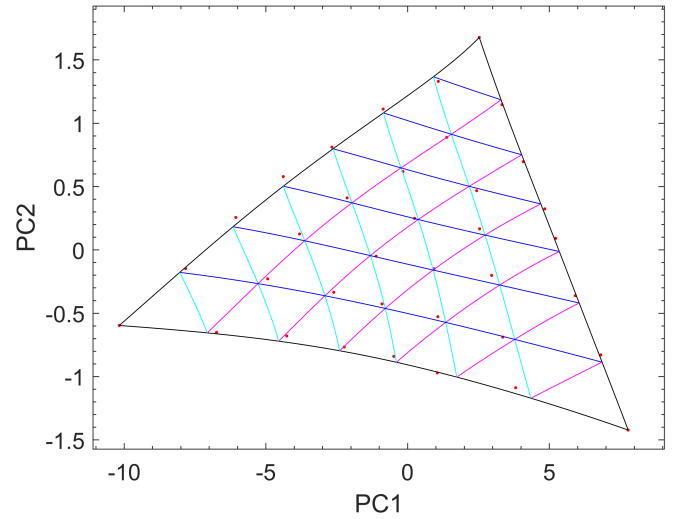
In this work, we will ignore the anisotropic effects of the bidirectional reflectance and assume that the measured bidirectional reflectance is a scaled version of the hemispherical reflectance. In a linear mixture, random scaling effects can be removed by projecting the spectrum generated by the linear model and the test spectrum \mathbf{y}_i on the unit sphere and minimizing the reconstruction error between them: $\left\| \frac{\mathbf{y}_i}{\|\mathbf{y}_i\|} - \frac{\mathbf{E}\mathbf{a}_i}{\|\mathbf{E}\mathbf{a}_i\|} \right\|^2$, s.t. $\sum_j a_j = 1, \forall j : a_j \geq 0$. From the obtained abundances, a reconstructed spectrum $\hat{\mathbf{y}}_i = \mathbf{E}\mathbf{a}_i$ is obtained.

When the mixture is nonlinear, our proposed approach is to scale the measured spectrum such that it lies closest to the one reconstructed by the linear model. This is done by minimizing: $\|s_r \mathbf{y}_i - \hat{\mathbf{y}}_i\|^2$, s.t. $s_r > 0$. The corrected spectral reflectance of the input spectrum \mathbf{y}_i is then given by $s_r \mathbf{y}_i$. In Fig. 3(b), the data manifold of the ternary mixture after correction is shown.

2) *Tackling spectral variability caused by variations in acquisition conditions*: For any supervised method, the major challenge is to make the learned model generalizable to a dataset acquired at different acquisition conditions. In remote sensing, the measured directional reflectance is dependent on the incident and reflectance angle, causing scaling effects on the measured reflectance. Topographical variations



(a)



(b)

Fig. 3: PCA reduced data manifold (ASD spectroradiometer) of ternary mixtures of Kaolin, Red clay, and $\text{Ca}(\text{OH})_2$; (a) Before removing random scaling effects; (b) After removing random scaling effects. The curves represent the reconstructed data manifold with the Bézier approach.

cause similar effects. Variations due to sensor type and white calibration panel often cause wavelength-dependent effects in the measured dataset [65]. Since white calibration and spectral calibration contain only linear operations [66], an affine transformation is sufficient to learn the relationship between two data manifolds.

Therefore, we can assume that, although the spectral reflectance of the same sample acquired at different acquisition conditions lies on different data manifolds, the relationship between these manifolds is linear:

$$\mathbf{x}_1 = \mathbf{T}\mathbf{x}_2 + \mathbf{b}, \quad (12)$$

where \mathbf{x}_1 and \mathbf{x}_2 represent the spectrum of a mixture in data manifold 1 and 2 respectively, \mathbf{T} is an invertible matrix and \mathbf{b}

represents a translation vector. Both \mathbf{T} and \mathbf{b} can be combined to define an affine transformation matrix:

$$\begin{bmatrix} \mathbf{x}_1 \\ 1 \end{bmatrix} = \begin{bmatrix} \mathbf{T} & \mathbf{b} \\ \mathbf{0}^T & 1 \end{bmatrix} \begin{bmatrix} \mathbf{x}_2 \\ 1 \end{bmatrix} \quad (13)$$

where $\mathbf{0}$ is a vector containing zeros.

We now assume that we have a manifold containing training data (i.e., the control points and their fractional abundances), and a test data point that lies on a different manifold, due to spectral variability (e.g., a mixture measured by another sensor). To estimate the affine transformation matrix between these 2 manifolds, we require the endmember spectra of both manifolds. The endmembers of the training manifold and the endmembers of the test manifold are denoted as $\mathbf{E}^{\text{train}}$ and \mathbf{E}^{test} , respectively. We also require the incenters of the linear simplices spanned by these endmembers. The incenter \mathbf{c} of a linear simplex spanned by p endmembers is the center of the largest possible hypersphere that can be inscribed in the simplex [67]. The fractional abundances of the incenter are given by:

$$a_j^c = \frac{V_j}{\sum_{k=1}^p V_k}, \quad (14)$$

where V_j is the volume of the sub simplex spanned by $\mathbf{E}_j = [\mathbf{e}_1, \dots, \mathbf{e}_{j-1}, \mathbf{e}_{j+1}, \dots, \mathbf{e}_p]$:

$$V_j = \sqrt{\frac{(-1)^{p-1} \cdot \text{cmd}(\mathbf{E}_j)}{2^{p-2}(p-2)!}},$$

where cmd is the cayley menger determinant,

$$\text{cmd}(\mathbf{E}_j) = \det \begin{pmatrix} 1 & 1 & 1 & \dots & 1 & 1 & \dots & 1 \\ 0 & d_{1,2}^2 & d_{1,3}^2 & \dots & d_{1,j-1}^2 & d_{1,j+1}^2 & \dots & d_{1,p}^2 \\ 1 & d_{2,1}^2 & 0 & \dots & d_{2,j-1}^2 & d_{2,j+1}^2 & \dots & d_{2,p}^2 \\ \vdots & \vdots & \vdots & \ddots & \vdots & \vdots & \ddots & \vdots \\ 1 & d_{j-1,1}^2 & d_{j-1,2}^2 & \dots & 0 & d_{j-1,j+1}^2 & \dots & d_{j-1,p}^2 \\ 1 & d_{j+1,1}^2 & d_{j+1,2}^2 & \dots & d_{j+1,j-1}^2 & 0 & \dots & d_{j+1,p}^2 \\ \vdots & \vdots & \vdots & \ddots & \vdots & \vdots & \ddots & \vdots \\ 1 & d_{p,1}^2 & d_{p,2}^2 & \dots & d_{p,j-1}^2 & d_{p,j+1}^2 & \dots & 0 \end{pmatrix}$$

where $d_{m,k}^2$ is the Euclidean distance between endmembers \mathbf{e}_m and \mathbf{e}_k . The incenter of the data simplex is then given by $\mathbf{c} = \mathbf{E}\mathbf{a}^c$.

Because, the transformation between the training and test manifolds cannot be performed directly in the reflectance space, we will describe the manifolds in a PCA-reduced space. The dimension of the PCA reduced space is defined by the number of endmembers. The transformation between the training and test manifolds is obtained by minimizing the following equation:

$$\arg \min_{\mathbf{T}, \mathbf{b}} \left\| \begin{bmatrix} \text{PCA}(\mathbf{E}^{\text{train}})^T \mathbf{E}^{\text{train}} & \text{PCA}(\mathbf{E}^{\text{train}})^T \mathbf{c}^{\text{train}} \\ \mathbf{1}^T & 1 \end{bmatrix} - \begin{bmatrix} \mathbf{T} & \mathbf{b} \\ \mathbf{0}^T & 1 \end{bmatrix} \begin{bmatrix} \text{PCA}(\mathbf{E}^{\text{test}})^T \mathbf{E}^{\text{test}} & \text{PCA}(\mathbf{E}^{\text{test}})^T \mathbf{c}^{\text{test}} \\ \mathbf{1}^T & 1 \end{bmatrix} \right\|_F^2 \quad (15)$$

where $\mathbf{c}^{\text{train}}$ and \mathbf{c}^{test} denote the incenters of the training and test data simplices, $\mathbf{1}$ is a vector containing p ones and the operator PCA estimates the p principal components of the input matrix.

Algorithm 1: Bézier supervised unmixing (BSU)

Input: $\mathbf{Y}^{\text{train}}(\{y_i\}_{i=1}^N \in \mathbf{R}_+^d)$, $\mathbf{E}^{\text{train}}(\{\mathbf{e}_l\}_{l=1}^p \in \mathbf{R}_+^d)$,

$\mathbf{Y}^{\text{test}}(\{y_i\}_{i=1}^M \in \mathbf{R}_+^f)$, $\mathbf{E}^{\text{test}}(\{\mathbf{e}_l\}_{l=1}^p \in \mathbf{R}_+^f)$

Output: $\hat{\mathbf{Y}}^{\text{test}}(\{y_i\}_{i=1}^M \in \mathbf{R}_+^d)$, $\hat{\mathbf{A}}^{\text{test}}(\{\mathbf{a}_i\}_{i=1}^M \in \mathbf{R}_+^p)$

Manifold transformation (Begin)

Estimate the affine transformation matrix between the training and test data manifolds (see Eq. (15))

Manifold transformation (End)

for $o \leftarrow 1$ **to** M

$\hat{\mathbf{A}}_o^{\text{test}}$: = Estimate the fractional abundance of each test sample by applying Eq. (16)

$\hat{\mathbf{Y}}_o^{\text{test}}$: = Reconstruct the spectral reflectance of each test sample by applying Eq. (7)

C. Bézier supervised unmixing

Once the transformation matrix is estimated, the proposed method estimates the fractional abundances of the mixture from the test manifold by minimizing the following optimization equation:

$$\hat{\mathbf{a}} = \arg \min_{\mathbf{a}} \left\| \begin{bmatrix} \mathbf{T} & \mathbf{b} \\ \mathbf{0}^T & 1 \end{bmatrix} \begin{bmatrix} \text{PCA}(\mathbf{E}^{\text{test}})^T \mathbf{y}^{\text{test}} \\ 1 \end{bmatrix} - \begin{bmatrix} \text{PCA}(\mathbf{E}^{\text{train}})^T \sum_i \sum_j \sum_k \frac{n!}{i!j!k!} a_1^i a_2^j a_3^k \mathbf{C}_{i,j,k} \\ 1 \end{bmatrix} \right\|^2 \quad (16)$$

s.t. : $\sum_{l=1}^p a_l = 1, \forall l : a_l \geq 0$

The proposed methodology will be referred to as Bézier supervised unmixing (**BSU**). The pseudo-code of the proposed method is shown in Algorithm 1.

IV. HYPERSPECTRAL DATA DESCRIPTION

1) *Relab dataset*: This dataset comprises spectra of carefully crafted mineral mixtures from the NASA Reflectance Experiment Laboratory (RELAB) at Brown University [68]. The selected binary mixtures involve five minerals: Alunite (Al), Anorthite (An), Bronzite (Br), Olivine (Ol), and Quartz (Qz). The binary combinations include An-Br, Br-Ol, Ol-An, and Qz-Al, each offering three mixtures with mass ratios of approximately 25%, 50%, and 75%. It's worth noting that these minerals share comparable grain sizes (around 100 μm) and densities (approximately 3 g/cm^3), resulting in volumetric and areal fractional abundances that closely align with these mass ratios. Fig. 4 shows endmembers obtained from the Relab dataset. The rationale behind choosing these mixtures is that the Hapke model accurately estimates their fractional abundances.

2) *Simulated Dataset*: A simulated hyperspectral dataset comprising 450 \times 450 pixels (see Fig. 5(b)) is generated through the nonlinear combination of five endmembers (as shown in Fig. 5 (a)). The spectral reflectances of five pure materials (Kaolin, roof clay, red clay, mixed clay, and $\text{Ca}(\text{OH})_2$) are acquired by a PSR-3500 spectral evolution spectrometer. This sensor generates spectra of 1024 bands, ranging from 345 nm to 2504 nm with a step size of 2 nm. The Hapke model serves as the nonlinear mixing model in this context.

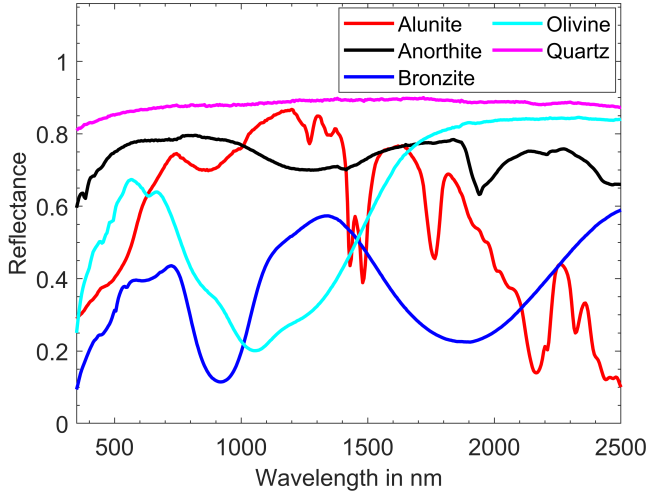


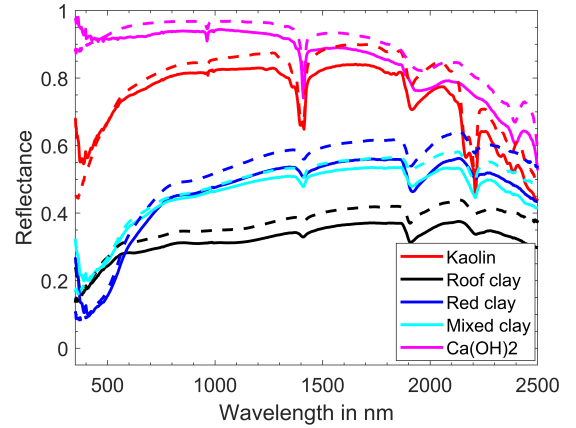
Fig. 4: Endmembers obtained from the Relab dataset.

This hyperspectral image contains 36 squares of 25×25 pixels with different randomly chosen quinary mixtures. The remaining background pixels also have random fractional abundances. Because the proposed method requires ground truth control points (spectra), another set of Hapke simulated spectra is generated by utilizing endmembers acquired by an ASD spectroradiometer (see Fig. 5 (a)). The ASD spectroradiometer produces spectra with 2151 bands, covering a range from 350 nm to 2500 nm, and bands are spaced 1 nm apart. This simulated dataset is applied to generate a 7th-order Bézier surface.

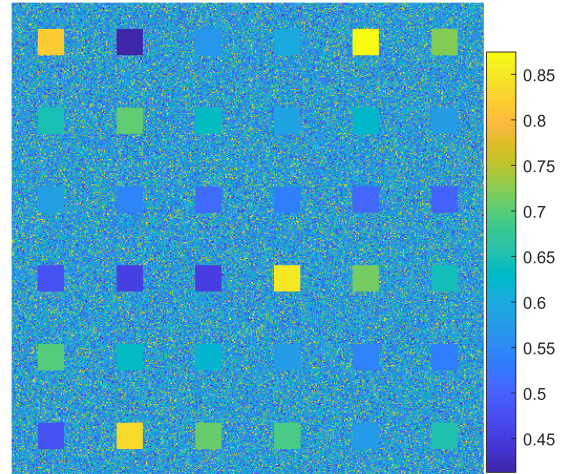
3) Multisensor hyperspectral dataset of intimate mixtures:

In [65], we prepared an extensive multisensor hyperspectral dataset of intimate mixtures by homogeneously mixing five pure clay powders, i.e., Kaolin, Roof clay, Red clay, mixed clay, and $\text{Ca}(\text{OH})_2$. We prepared a total of 325 mixtures. To prepare these mixtures, all possible clay combinations were considered, i.e., 10 binary combinations, 10 ternary combinations, 5 quaternary combinations, and one quinary combination. The ground truth fractional abundances of these mixtures uniformly cover the five-dimensional simplex, with a step size of 14.286 % mass ratios. The generated samples correspond to the control points of a Bézier surface of order 7. In the case of binary clay combinations, six distinct mixtures were created for each combination. For ternary, quaternary, and quinary clay combinations, we generated 15, 20, and 15 unique mixtures, respectively. We refer again to Figure 1, where the uniformly sampled fractional abundances for a ternary clay combination were presented. The three different types of clay are situated at the vertices of the simplex, where all binary mixtures are located along the lines connecting two types of clay, while ternary mixtures are found within the interior of the simplex. Even though ground truth fractional abundances were given by construction, X-ray powder diffraction, and X-ray fluorescence elemental analysis were performed to verify that the generated intimate mixtures were sufficiently homogeneous.

These 325 mixtures and five pure clay powders were



(a)



(b)

Fig. 5: Simulated dataset: a) Endmembers acquired by PSR-3500 spectral evolution (full line) and ASD spectroradiometer (dashed line) b) Band number 640 (1451 nm) of the simulated image.

scanned with both the ASD spectroradiometer and the PSR-3500 spectral evolution spectroradiometer. The spectral reflectances of the five pure clay samples acquired by these two different sensors are shown in Fig. 5(a). The radiance spectra from the intimate mixtures acquired by these sensors were converted into reflectance by calibration with a white calibration panel.

Given that the distance between the sample and the sensors in handheld devices is only a few centimeters, differences in sample compaction and clay densities cause slight variations in sample height of the order of a few millimeters, leading to a scaling effect in the measured spectra. These scaling effects are taken care of by the proposed procedure to tackle random scaling effects.

V. EXPERIMENTS AND RESULTS

The performance of BSU was evaluated and compared with the following unmixing methods: Linear unmixing: FCLSU [2], Bilinear unmixing: PPNM [18] and nonnegative tensor

factorization (LR-NTF) [30], Multilinear unmixing: MLM [21], the neighbor-band ratio unmixing approach NBRU [61], and the Hapke model [27]. For these six methods, the utilized endmembers are the ones, acquired by the hyperspectral sensors. The proposed approach BSU uses training samples from one sensor as control points to generate a Bézier surface.

All quantitative comparisons are provided by the abundance root mean squared error, i.e. the error between the estimated fractional abundances ($\hat{\mathbf{A}}$) and the ground truth fractional abundances (\mathbf{A}):

$$\text{Abundance RMSE (AE)} = \sqrt{\frac{1}{pn} \sum_{k=1}^p \sum_{i=1}^n (\hat{\mathbf{A}}_{ki} - \mathbf{A}_{ki})^2} \times 100 \quad (17)$$

where p and n denote the number of endmembers and the number of mixed spectra, respectively.

We have performed experiments under two distinct experimental conditions, each demanding unique applications of the datasets. In the first experimental condition, no sensor-specific variability is introduced. In the second experimental condition, the proposed method is validated for its invariance to spectral variability caused by applying different sensors.

A. Experimental condition 1: no variability in acquisition conditions

1) *Relab dataset*: In the first experiment, the goal is to unmix the binary intimate mixtures of the Relab dataset. The training samples that are required to generate Bézier surfaces are produced by utilizing the Hapke model. In the next step, the fractional abundances of the real binary mixtures (see Section IV-1) are estimated by applying Eq. (8). In Fig. 6, we show the obtained AE with respect to the order of the Bézier surface. As expected, the error decreases when the order of the Bézier surface increases. The AE obtained by the Hapke model on this dataset is also shown for comparison. Except for the binary mixture of Quartz and Alunite, the proposed method can compete with the Hapke model itself using Bézier surfaces of order less than 10. Since the Hapke model was used to generate the Bezier surface, the results in principle at best approach those of the Hapke model itself. However, because the Hapke model does not perfectly explain the Relab data, our approach may outperform it. We applied a Bézier surface of order 7 to estimate the fractional abundances of the real binary mixtures and compared the results with the mixing models (FCLSU, PPNM, LR-NTF, MLM, NBRU, and Hapke model). Table I shows the AE of the competing methods. Except for the Hapke model, NBRU, and BSU, none of the methods could perform well for this dataset. It's noteworthy to observe that the proposed method outperforms the Hapke model on the Ol-An binary mixtures.

Real-life applications on material recognition require one Bézier surface that can characterize most of the mixtures of interest. In that case, the method has to accurately estimate the fractional abundances of mixtures without having prior knowledge of the number of endmembers in the mixture. A non-zero estimated abundance value for a certain material then denotes the presence of that material in the mixture.

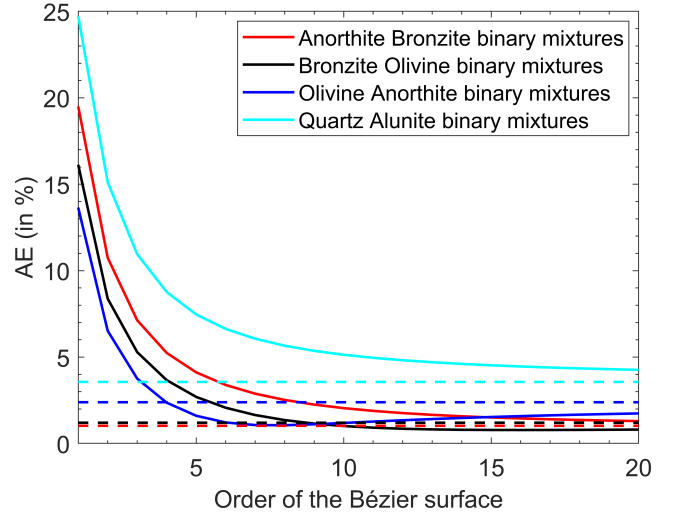


Fig. 6: Relab data: AE obtained by the proposed method in function of the order of the Bézier surface (full line) and the Hapke model (dashed line).

TABLE I: AE of the unmixing methods on the binary intimate mixtures of the Relab dataset. The best performances are shown in bold.

	FCLSU	PPNM	LR-NTF	MLM	NBRU	Hapke	BSU
An-Br	19.50	22.61	21.26	19.50	4.95	1.03	2.89
Br-Ol	16.13	13.95	13.13	13.05	3.61	1.21	1.65
Ol-An	13.65	13.20	9.99	11.21	3.89	2.39	1.07
Qz-Al	24.73	26.25	27.77	24.73	14.48	3.57	6.07

To demonstrate the effectiveness of this approach, in the next experiment, we applied the Hapke model to generate a 5-endmember data-manifold, with the endmembers from which the measured binary mixtures are generated. In the next step, a Bézier surface of 7th-order is produced from this simulated data, after which the proposed method is validated on all true binary mixtures, without having prior knowledge of which endmembers form the binary mixtures. In Fig. 7, we show the estimated fractional abundances by the proposed method overlaid on the ternary diagram with An, Br, and Ol as endmembers. In the figure, the red arrows point to the true position of the fractional abundances. As can be observed, the estimated fractional abundances lie close to the true ones on the ternary diagram. Additionally, the estimated abundances align with the faces (lines connecting binary mixtures) of the ternary diagram. For comparison, the results of the FCLSU, PPNM, LR-NTF, MLM, NBRU, and Hapke model, with all 5 minerals as endmembers, are shown in Table II. Except for the Hapke model and NBRU none of the mixing models could perform well for this dataset.

TABLE II: AE of the unmixing methods on the binary intimate mixtures of the Relab dataset, when all 5 minerals are used as endmembers. The best performances are shown in bold.

	FCLSU	PPNM	LR-NTF	MLM	NBRU	Hapke	BSU
Al-An-Br-Ol-Qz	13.25	12.91	13.33	12.72	5.26	2.18	2.54

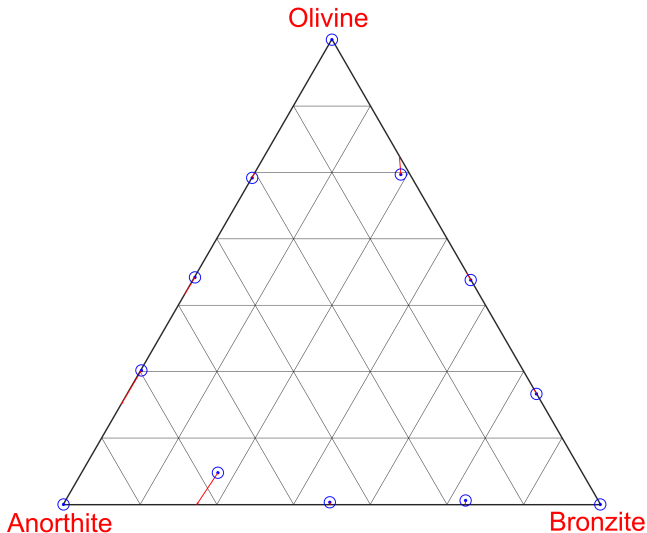


Fig. 7: Relab data: unmixing results of proposed method overlaid on the ternary diagram with Anorthite, Bronzite, and Olivine as endmembers. Here, the red arrows point to the true position of the fractional abundances.

As mentioned in the methodology section, the proposed method not only accurately estimates the fractional abundances but can also accurately reconstruct spectral reflectances of mixtures. In Fig. 8, we show reconstructed spectra (dashed lines) by the proposed method overlaid on the true ones (full lines) for the Relab data. As expected, the reconstructed spectra perfectly match the true ones.

2) *Multisensor hyperspectral dataset*: In the following experiment, we use the ASD spectroradiometer dataset. All mixtures serve as control points to generate a 7th-order Bézier surface. In Fig. 9, we show an example generated data manifold of ternary mixtures of Kaolin, Red clay, and $\text{Ca}(\text{OH})_2$. From the generated 7th-order Bézier surface, the control points required to generate Bézier surfaces of orders between 1-7 are extracted. Then, the fractional abundances of the true mixtures are estimated by applying Eq. (8).

In Fig. 10, we show the mean AE (average over different clay combinations) with respect to the order of the Bézier surface. Except for the quinary mixtures (only one clay combination), standard deviations are shown as well. Similar to the results on the Relab dataset, the error decreases when the order of the Bézier surface increases.

B. Experimental condition 2: variability in acquisition conditions

In the second group of experiments, we validate the approach to situations with spectral variability due to the use of different sensors.

1) *Simulated dataset*: In this experiment, the simulated image (generated by the PSR-3500 spectral evolution endmembers and the Hapke model, see Fig. 5(a)) is unmixed using the proposed approach. In order to investigate the robustness of the proposed method in the presence of noise, Gaussian noise at different signal-to-noise ratio (SNR) levels was added

to the spectra. The training data is provided by the manifold generated by the ASD spectroradiometer endmembers (see Fig. 5(a)) and the Hapke model. In Fig. 11, we show the estimated abundance maps and the absolute difference between ground truth and estimated maps (SNR=50 dB). For a comparison, the abundance maps estimated by FCLSU, PPNM, and MLM are shown as well. As can be observed, except for the proposed method, none of the competing methods could produce accurate abundance maps. Table III shows the obtained AE's on this dataset. As can be observed, the proposed method considerably outperforms the competing techniques. This demonstrates that the proposed approach is able to tackle spectral variability caused by the use of different sensors. The error of the proposed method increases for SNR values lower than 40 dB. To further improve the performance of the proposed method in high noise scenarios, a denoising algorithm such as a parameter-free hyperspectral restoration technique ([69]) can be used as a preprocessing tool. After applying this method, we managed to decrease the error of the proposed method from 10.11% to 4.19% for the dataset with SNR of 30 dB.

TABLE III: AE of the unmixing methods on the simulated dataset for different noise levels. The best performances are shown in bold.

	FCLSU	PPNM	LR-NTF	MLM	NBRU	BSU
30dB	14.62	15.41	15.14	14.82	26.52	10.11
35dB	14.46	14.41	14.89	14.50	25.08	7.38
40dB	14.66	14.40	15.12	14.64	23.64	4.78
45dB	14.80	15.51	15.37	14.78	19.74	4.52
50dB	14.82	14.58	15.47	14.80	15.60	3.36

2) *Multisensor hyperspectral dataset*: In the final experiment, the generated Bézier surfaces are obtained by control points from the ASD spectroradiometer dataset and the method is validated on the mixtures from the PSR-3500 spectral evolution spectrometer. In Table IV, the results for all the mixtures are shown. For a comparison, the results of the FCLSU, PPNM, LR-NTF, MLM, NBRU, and Hapke models are shown as well. As can be observed, the proposed method outperforms the competing techniques. Even though the Hapke model was developed to characterize intimate mixtures, its performance was the lowest among the competing methods. In Fig. 12, we show estimated fractional abundances on the PSR-3500 spectral evolution spectrometer data overlaid on the ternary diagram of the mixtures of Kaolin, Mixed clay, and $\text{Ca}(\text{OH})_2$. As can be observed, except for a few mixtures, the estimated fractional abundances are close to the true ones. For these ternary mixtures, the AE is 4.85 %.

VI. DISCUSSION

From the experiments, the following general conclusions can be drawn:

- In general, the LMM is not suitable for describing the spectral reflectances of intimate mixtures of mineral powders. Its AE for intimate mixtures varies between 10-25 %.

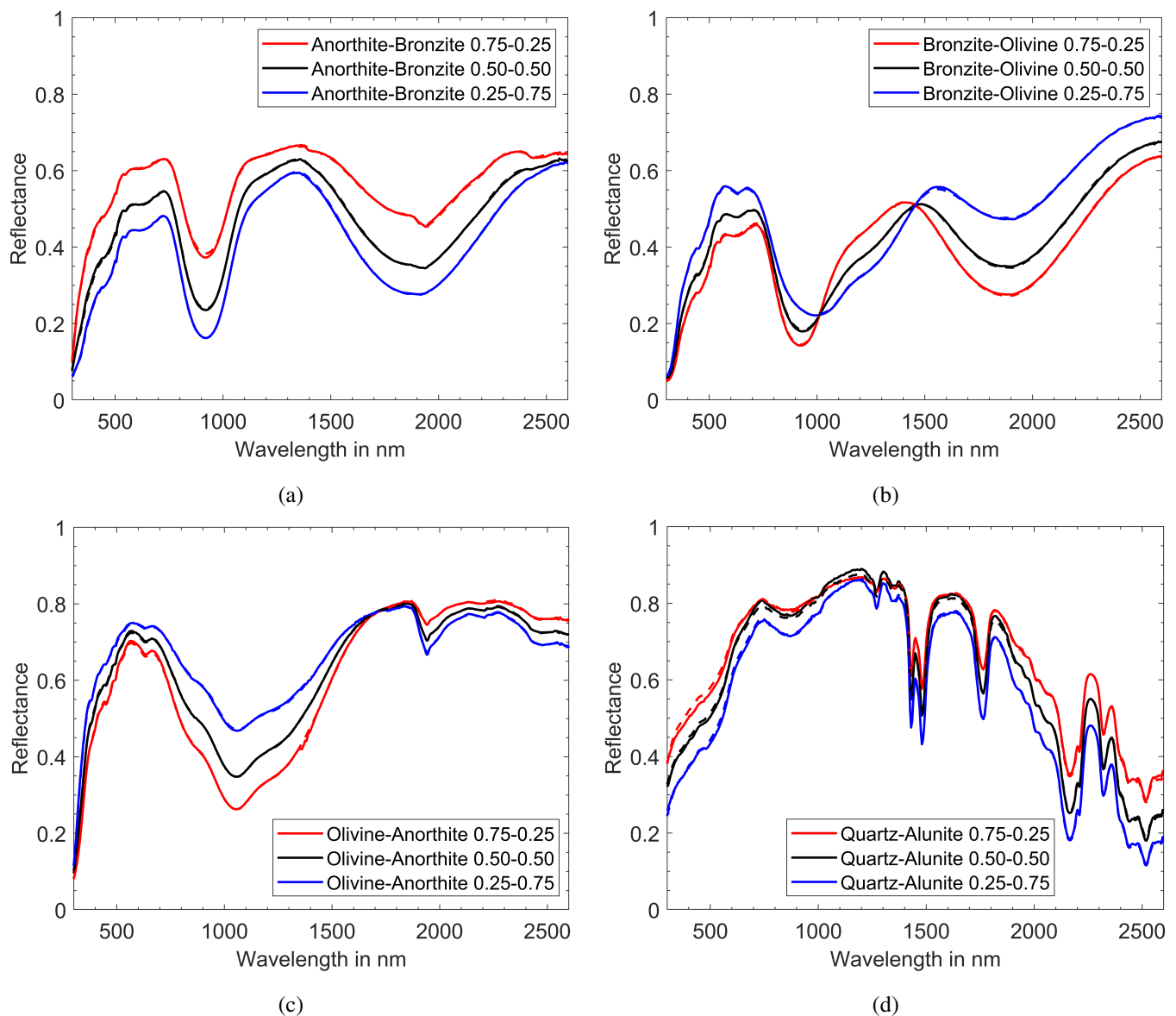


Fig. 8: Relab data: reconstructed spectra (dashed lines) versus true ones (full lines). (a) Anorthite and Bronzite binary mixtures; (b) Bronzite and Olivine binary mixtures; (c) Olivine and Anorthite binary mixtures; (d) Quartz and Alunite binary mixtures.

TABLE IV: Mean AE of the unmixing methods on the PSR-3500 spectral evolution spectrometer dataset. The best performances are shown in bold.

	FCLSU	PPNM	LR-NTF	MLM	NBRU	Hapke	BSU
Binary	7.05	5.44	7.39	6.57	12.48	15.50	5.12
Ternary	9.77	9.93	9.45	8.84	15.09	22.64	5.80
Quaternary	10.80	11.55	10.30	10.01	15.30	22.02	6.27
Quinary	11.02	11.04	10.62	10.43	15.03	18.34	9.75

- Similar to the LMM, the bilinear models, such as PPNM and LR-NTF, did not perform well in estimating the fractional abundances of intimate mixtures. This suggests that these models cannot accurately describe the interaction of light with intimate mixtures.
- Even though the MLM outperformed the LMM for esti-

ating fractional abundances of some intimate mixtures, the obtained AE's are still too large to rely on the method.

- The Hapke model can accurately estimate the fractional abundances of intimate mixtures only when the particles are significantly larger than the wavelength of light, are spherical, and scatter light isotropically. These criteria are fulfilled by the Relab dataset (see Section V-A1), resulting in an excellent performance on this dataset. On the other hand, it could not outperform the LMM on the Multisensor hyperspectral dataset of intimate mixtures (see Section V-B2). This result suggests that the Hapke model is less suitable for analyzing more complex mixtures.
- While NBRU outperformed the FCLSU, PPNM, LR-NTF, and MLM models on the Relab dataset, its performance on the other datasets did not exhibit a significant

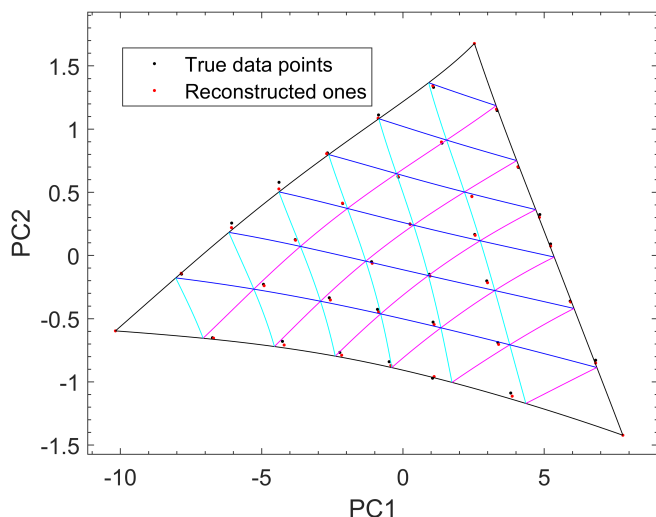


Fig. 9: PCA reduced data manifold (ASD spectroradiometer) of ternary mixtures of Kaolin, Red clay, and $\text{Ca}(\text{OH})_2$. Here, black dots denote the true data points, while red dots denote reconstructed ones.

improvement over these models.

- BSU outperformed the other techniques in all experiments except on the Relab dataset (see Section V-A1) where the Hapke model slightly outperformed BSU, the reason being that the Hapke model itself was used to generate the Bézier surface in that experiment. Although the performance of the proposed method could be enhanced by employing a higher-order Bézier surface (see Fig. 6), for the sake of consistency, the order of the Bézier surface was set to 7 for all the experiments.
- Unlike the current nonlinear mixing models, BSU demonstrated its capability to address both nonlinearity and spectral variability concurrently (see Section V-B).
- The proposed method not only accurately estimated the fractional abundances of intimate mixtures but also accurately reconstructed their spectral reflectances (see Fig. 8). This displays the effectiveness of the developed methodology.
- The major obstacle for implementing the proposed method in real-life applications lies in generating a sufficient number of control points to accurately characterize the Bézier surface. A general n^{th} order Bézier surface has $\frac{(n+p-1)!}{n!(p-1)!}$ control points. Even though prior information regarding the endmembers is often available, the required order of a Bézier surface is governed by the complexity of the mixtures. Based on our extensive experiments, we found that a Bézier surface of order $n = 7$ is sufficient for the majority of intimate mixtures. When the nonlinearity of the mixture is low, essentially constituting an almost linearly mixed dataset, the 7th-order Bézier surface simplifies to the linear simplex (see Eq. 11), requiring only the p endmembers as control points.
- Despite the potential for using this method for material recognition, the significant uncertainty in the estimated fractional abundances (1-9%) by the proposed method presents a challenge for accurately detecting targets with low fractional abundances ($<1\%$) in intimate mixtures.
- In the experimental section, we employed two approaches to generate control points: a) Simulation of spectral reflectance of intimate mixtures: On the Relab dataset, the Hapke model was utilized to simulate the spectral reflectances of the control points. The generated surface was validated on the measured dataset; b) Generation of real intimate mixtures: When the interaction of light with the mixtures can not be described by a mixture model, real mixtures prepared in a laboratory setting are required. In our work, we generated real intimate mixtures by homogeneously mixing pure clay powders. The spectral reflectances of the control points are then acquired by a sensor of choice to generate the Bézier surface. For data acquired under different acquisition conditions, no control points, except for the endmembers are required, as the manuscript describes a procedure to map this data manifold to the generated Bézier surface.
- In theory, the method should be applicable in remote sensing settings, by transforming a data manifold to one that is generated in lab conditions. However, this comes with great challenges. First, it should be known which materials are present, and their endmember spectra should be available. Moreover, intrinsic spectral variability between the datasets should be minimal, and most importantly, there is no way of validating the obtained results, because there is no ground truth available. Creating ground truth references for nonlinear unmixing of real spaceborne and airborne hyperspectral remote sensing images is a very difficult and challenging task. Overcoming this obstacle is essential for making the method directly applicable in remote sensing settings. One potential solution lies in simulating the spectral reflectances of the required control points. This can be achieved through the use of physically based Ray-Tracing models [70]. On the other hand, advanced radiative transfer models exist in the literature that can describe the interaction of light with intimate mixtures, such as soils and geological samples. While these models may lack invertibility, they remain useful for simulating spectral reflectances of control points. In future work, we will explore the possibility of integrating the proposed method with these models to unmix remote sensing data.
- All methods were developed in MATLAB and ran on an Intel Core i9-12900KF CPU, 3.19 GHz machine with 16 cores. The runtime for all unmixing methods applied to the Relab dataset (17 mixtures), the Simulated dataset ($450 \times 450 = 202500$ mixtures), and the Multisensor hyperspectral dataset (330 mixtures) is presented in Table V. FCLSU stands out as the fastest algorithm, while LR-NTF was slowest among the evaluated techniques. The generation of a 7th-order Bézier surface for the five endmember mixtures (Simulated dataset) using the proposed method took less than one second. Additionally, the estimation of the fractional abundances required approximately 4.5 milliseconds for each test sample.

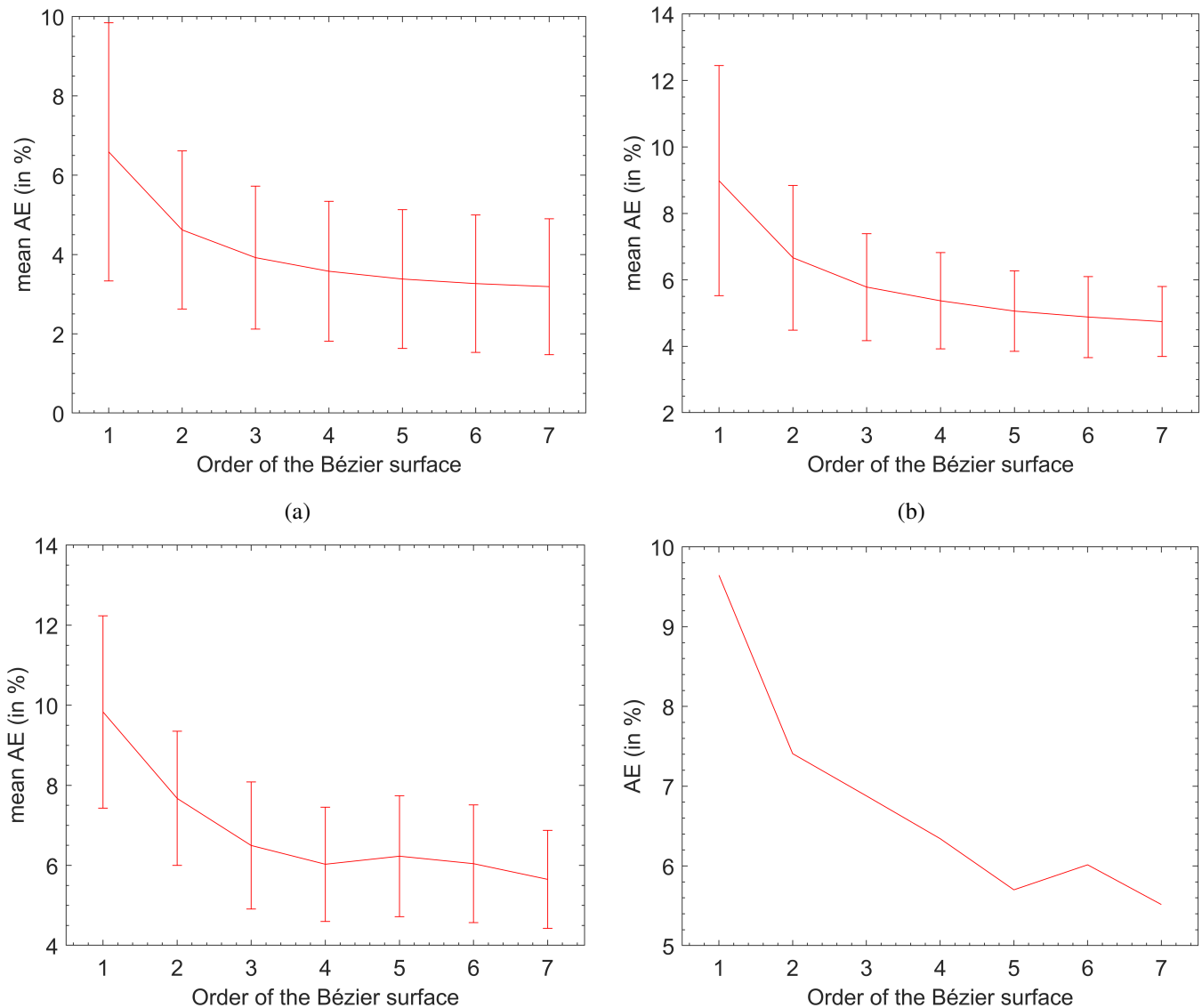


Fig. 10: AE (ASD Spectroradiometer) obtained by the proposed method in function of the order of the Bézier surface. (a) Binary mixtures; (b) Ternary mixtures; (c) Quaternary mixtures; (d) Quinary mixtures.

TABLE V: Processing time (in seconds) of the unmixing techniques applied to different datasets.

	FCLSU	PPNM	LR-NTF	MLM	NRBU	Hapke	BSU
Relab	0.001	0.05	0.78	0.03	0.09	0.10	0.34
Simulated	16.26	652.80	15762.55	775.29	2880.39	-	898.40
Multisensor	0.02	0.92	20.40	0.62	4.83	2.46	4.06

VII. CONCLUSION

This paper introduces a methodology designed for the precise estimation of fractional abundances in intimate mixtures, with an additional feature of invariance to variations in acquisition conditions. The proposed approach is a supervised approach that characterizes the nonlinear data manifolds by high-dimensional Bézier surfaces. Validation of the proposed method was conducted on datasets generated under laboratory conditions and in cross-sensor scenarios. The results showed

that the proposed method not only accurately estimated the fractional abundances of intimate mixtures but also faithfully reconstructed their spectral reflectances in different unmixing scenarios including, single sensor, spectral variability, and multiple sensors for intimate mixtures of up to five materials confirming the generalization ability of the proposed method. The experimental results confirmed that the proposed method simultaneously copes with the nonlinearity and spectral variability. This demonstrated the effectiveness of the proposed methodology.

ACKNOWLEDGEMENT

The research presented in this paper is funded by the Research Foundation-Flanders - project G031921N. Bikram Koirala is a postdoctoral fellow of the Research Foundation Flanders, Belgium (FWO: 1250824N-7028).

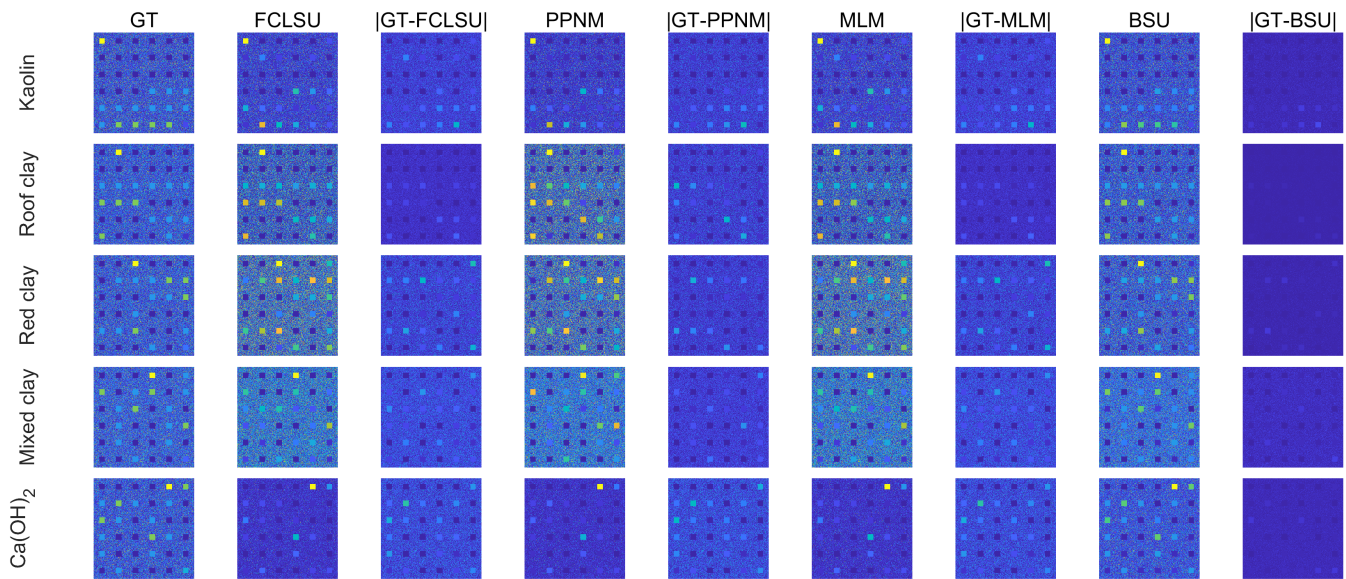


Fig. 11: Simulated dataset (SNR 50dB)- Ground truth (GT), estimated abundance maps, and absolute difference with the GT for the four different unmixing methods on the Hapke simulated dataset.

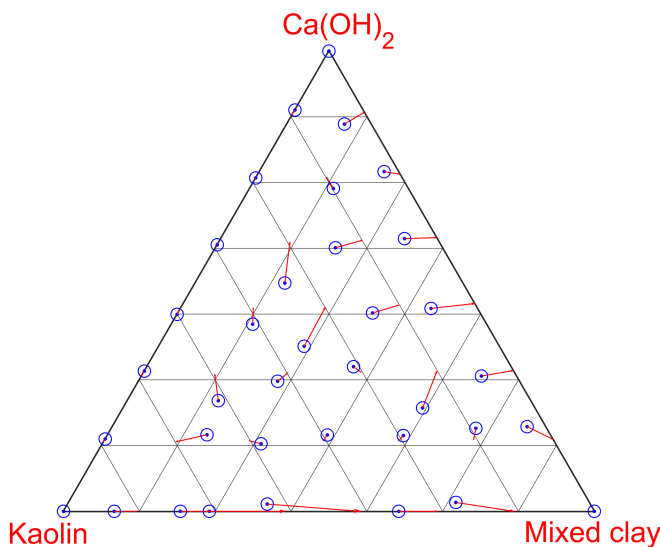


Fig. 12: Unmixing results (PSR-3500 spectral evolution spectrometer) overlaid on the ternary diagram of the mixtures of Kaolin, Mixed clay, and $\text{Ca}(\text{OH})_2$. Here, the red arrows point to the true position of the fractional abundances.

REFERENCES

- [1] N. Keshava and J. F. Mustard, "Spectral unmixing," *IEEE Signal Processing Magazine*, vol. 19, no. 1, pp. 44–57, Jan 2002.
- [2] J. W. Boardman, "Geometric mixture analysis of imaging spectrometry data," in *IEEE International Geoscience and Remote Sensing Symposium (IGARSS)*, vol. 4, Aug 1994, pp. 2369–2371.
- [3] D. C. Heinz and Chein-I-Chang, "Fully constrained least squares linear spectral mixture analysis method for material quantification in hyperspectral imagery," *IEEE Transactions on Geoscience and Remote Sensing*, vol. 39, no. 3, pp. 529–545, 2001.
- [4] B. Palsson, J. R. Sveinsson, and M. O. Ulfarsson, "Blind hyperspectral unmixing using autoencoders: A critical comparison," *IEEE Journal of Selected Topics in Applied Earth Observations and Remote Sensing*, pp. 1–1, 2022.
- [5] Y. Su, A. Marinoni, J. Li, J. Plaza, and P. Gamba, "Stacked nonnegative sparse autoencoders for robust hyperspectral unmixing," *IEEE Geoscience and Remote Sensing Letters*, vol. 15, no. 9, pp. 1427–1431, 2018.
- [6] Y. Su, J. Li, A. Plaza, A. Marinoni, P. Gamba, and S. Chakravorty, "Daen: Deep autoencoder networks for hyperspectral unmixing," *IEEE Transactions on Geoscience and Remote Sensing*, vol. 57, no. 7, pp. 4309–4321, 2019.
- [7] R. A. Borsoi, T. Imbiriba, and J. C. M. Bermudez, "Deep generative endmember modeling: An application to unsupervised spectral unmixing," *IEEE Transactions on Computational Imaging*, vol. 6, pp. 374–384, 2020.
- [8] Q. Jin, Y. Ma, F. Fan, J. Huang, X. Mei, and J. Ma, "Adversarial autoencoder network for hyperspectral unmixing," *IEEE Transactions on Neural Networks and Learning Systems*, pp. 1–15, 2021.
- [9] M. Tang, Y. Qu, and H. Qi, "Hyperspectral nonlinear unmixing via generative adversarial network," in *IGARSS 2020-2020 IEEE International Geoscience and Remote Sensing Symposium*. IEEE, 2020, pp. 2404–2407.
- [10] Y. Qu and H. Qi, "udas: An untied denoising autoencoder with sparsity for spectral unmixing," *IEEE Transactions on Geoscience and Remote Sensing*, vol. 57, no. 3, pp. 1698–1712, 2019.
- [11] B. Palsson, M. O. Ulfarsson, and J. R. Sveinsson, "Convolutional autoencoder for spectral-spatial hyperspectral unmixing," *IEEE Transactions on Geoscience and Remote Sensing*, pp. 1–15, 2020.
- [12] L. Gao, Z. Han, D. Hong, B. Zhang, and J. Chanussot, "Cycu-net: Cycle-consistency unmixing network by learning cascaded autoencoders," *IEEE Transactions on Geoscience and Remote Sensing*, pp. 1–14, 2021.
- [13] B. Rasti, B. Koirala, P. Scheunders, and P. Ghamisi, "UnDIP: Hyperspectral unmixing using deep image prior," *IEEE Transactions on Geoscience and Remote Sensing*, pp. 1–15, 2021.
- [14] P. Ghosh, S. K. Roy, B. Koirala, B. Rasti, and P. Scheunders, "Hyperspectral unmixing using transformer network," *IEEE Transactions on Geoscience and Remote Sensing*, vol. 60, pp. 1–16, 2022.
- [15] B. Rasti, B. Koirala, P. Scheunders, and J. Chanussot, "Minsicnet: Minimum simplex convolutional network for deep hyperspectral unmixing," *IEEE Transactions on Geoscience and Remote Sensing*, pp. 1–1, 2022.
- [16] R. Heylen, M. Parente, and P. Gader, "A review of nonlinear hyperspectral unmixing methods," *IEEE Journal of Selected Topics in Applied Earth Observations and Remote Sensing*, vol. 7, no. 6, pp. 1844–1868, June 2014.
- [17] W. Fan, B. Hu, J. Miller, and M. Li, "Comparative study between a new nonlinear model and common linear model for analysing laboratory

- simulated-forest hyperspectral data,” *International Journal of Remote Sensing*, vol. 30, no. 11, pp. 2951–2962, 2009.
- [18] Y. Altmann, A. Halimi, N. Dobigeon, and J. Tourneret, “Supervised nonlinear spectral unmixing using a postnonlinear mixing model for hyperspectral imagery,” *IEEE Transactions on Image Processing*, vol. 21, no. 6, pp. 3017–3025, 2012.
- [19] A. Halimi, Y. Altmann, N. Dobigeon, and J. Tourneret, “Nonlinear unmixing of hyperspectral images using a generalized bilinear model,” *IEEE Transactions on Geoscience and Remote Sensing*, vol. 49, no. 11, pp. 4153–4162, 2011.
- [20] I. Meganem, P. Déliot, X. Briottet, Y. Deville, and S. Hosseini, “Linear–quadratic mixing model for reflectances in urban environments,” *IEEE Transactions on Geoscience and Remote Sensing*, vol. 52, no. 1, pp. 544–558, 2014.
- [21] R. Heylen and P. Scheunders, “A multilinear mixing model for nonlinear spectral unmixing,” *IEEE Transactions on Geoscience and Remote Sensing*, vol. 54, no. 1, pp. 240–251, Jan 2016.
- [22] A. Marinoni and P. Gamba, “A novel approach for efficient p -linear hyperspectral unmixing,” *IEEE Journal of Selected Topics in Signal Processing*, vol. 9, no. 6, pp. 1156–1168, Sep. 2015.
- [23] A. Marinoni, J. Plaza, A. Plaza, and P. Gamba, “Nonlinear hyperspectral unmixing using nonlinearity order estimation and polytope decomposition,” *IEEE Journal of Selected Topics in Applied Earth Observations and Remote Sensing*, vol. 8, no. 6, pp. 2644–2654, June 2015.
- [24] A. Marinoni, A. Plaza, and P. Gamba, “Harmonic mixture modeling for efficient nonlinear hyperspectral unmixing,” *IEEE Journal of Selected Topics in Applied Earth Observations and Remote Sensing*, vol. 9, no. 9, pp. 4247–4256, Sep. 2016.
- [25] B. Yang, B. Wang, and Z. Wu, “Nonlinear hyperspectral unmixing based on geometric characteristics of bilinear mixture models,” *IEEE Transactions on Geoscience and Remote Sensing*, vol. 56, no. 2, pp. 694–714, 2018.
- [26] B. Hapke, R. Nelson, and W. Smythe, “The opposition effect of the moon: Coherent backscatter and shadow hiding,” *Icarus*, vol. 133, no. 1, pp. 89 – 97, 1998.
- [27] B. Hapke, “Bidirectional reflectance spectroscopy: 1. theory,” *Journal of Geophysical research*, vol. 86, pp. 3039–3054, 1981.
- [28] M. Zhao, L. Yan, and J. Chen, “Lstm-dnn based autoencoder network for nonlinear hyperspectral image unmixing,” *IEEE Journal of Selected Topics in Signal Processing*, vol. 15, no. 2, pp. 295–309, 2021.
- [29] M. Zhao, M. Wang, J. Chen, and S. Rahardja, “Hyperspectral unmixing for additive nonlinear models with a 3-d-cnn autoencoder network,” *IEEE Transactions on Geoscience and Remote Sensing*, vol. 60, pp. 1–15, 2022.
- [30] L. Gao, Z. Wang, L. Zhuang, H. Yu, B. Zhang, and J. Chanussot, “Using low-rank representation of abundance maps and nonnegative tensor factorization for hyperspectral nonlinear unmixing,” *IEEE Transactions on Geoscience and Remote Sensing*, vol. 60, pp. 1–17, 2022.
- [31] T. Fang, F. Zhu, and J. Chen, “Hyperspectral unmixing based on multilinear mixing model using convolutional autoencoders,” *IEEE Transactions on Geoscience and Remote Sensing*, vol. 62, pp. 1–16, 2024.
- [32] M. Li, B. Yang, and B. Wang, “Emlm-net: An extended multilinear mixing model-inspired dual-stream network for unsupervised nonlinear hyperspectral unmixing,” *IEEE Transactions on Geoscience and Remote Sensing*, vol. 62, pp. 1–16, 2024.
- [33] M. Wang, M. Zhao, J. Chen, and S. Rahardja, “Nonlinear unmixing of hyperspectral data via deep autoencoder networks,” *IEEE Geoscience and Remote Sensing Letters*, vol. 16, no. 9, pp. 1467–1471, 2019.
- [34] B. Rasti, B. Koirala, and P. Scheunders, “Hapkecnn: Blind nonlinear unmixing for intimate mixtures using hapke model and convolutional neural network,” *IEEE Transactions on Geoscience and Remote Sensing*, vol. 60, pp. 1–15, 2022.
- [35] G. Foody, “Relating the land-cover composition of mixed pixels to artificial neural network classification output,” *Photogrammetric Engineering and Remote Sensing*, vol. 62, no. 5, p. 491–499, 1996.
- [36] G. Licciardi and F. D. Frate, “Pixel unmixing in hyperspectral data by means of neural networks,” *IEEE Transactions on Geoscience and Remote Sensing*, vol. 49, pp. 4163–4172, 2011.
- [37] B. Koirala, R. Heylen, and P. Scheunders, “A neural network method for nonlinear hyperspectral unmixing,” in *IEEE Intern. Geosci Remote Sens. Symp.*, 2018, pp. 4233–4236.
- [38] M. Koirala, B. and Khodadadzadeh, C. Contreras, Z. Zahiri, R. Gloaguen, and P. Scheunders, “A supervised method for nonlinear hyperspectral unmixing,” *Remote Sensing*, vol. 11, no. 20, p. 2458, Oct 2019.
- [39] B. Koirala, Z. Zahiri, A. Lamberti, and P. Scheunders, “Robust supervised method for nonlinear spectral unmixing accounting for endmember variability,” *IEEE Transactions on Geoscience and Remote Sensing*, vol. 59, no. 9, pp. 7434–7448, 2021.
- [40] L. Drumetz, J. Chanussot, C. Jutten, W. Ma, and A. Iwasaki, “Spectral variability aware blind hyperspectral image unmixing based on convex geometry,” *IEEE Transactions on Image Processing*, vol. 29, pp. 4568–4582, 2020.
- [41] L. Drumetz, J. Chanussot, and C. Jutten, “Chapter 2.7 - variability of the endmembers in spectral unmixing,” in *Hyperspectral Imaging*, ser. Data Handling in Science and Technology, J. M. Amigo, Ed. Elsevier, 2020, vol. 32, pp. 167 – 203.
- [42] B. Somers, G. P. Asner, L. Tits, and P. Coppin, “Endmember variability in spectral mixture analysis: A review,” *Remote Sensing of Environment*, vol. 115, no. 7, pp. 1603 – 1616, 2011.
- [43] A. Zare and K. C. Ho, “Endmember variability in hyperspectral analysis: Addressing spectral variability during spectral unmixing,” *IEEE Signal Processing Magazine*, vol. 31, no. 1, pp. 95–104, 2014.
- [44] D. Roberts, M. Gardner, R. Church, S. Ustin, G. Scheer, and R. Green, “Mapping chaparral in the santa monica mountains using multiple endmember spectral mixture models,” *Remote Sensing of Environment*, vol. 65, no. 3, pp. 267 – 279, 1998.
- [45] B. Somers, M. Zortea, A. Plaza, and G. P. Asner, “Automated extraction of image-based endmember bundles for improved spectral unmixing,” *IEEE Journal of Selected Topics in Applied Earth Observations and Remote Sensing*, vol. 5, no. 2, pp. 396–408, 2012.
- [46] T. Uezato, R. J. Murphy, A. Melkumyan, and A. Chlingaryan, “A novel endmember bundle extraction and clustering approach for capturing spectral variability within endmember classes,” *IEEE Transactions on Geoscience and Remote Sensing*, vol. 54, no. 11, pp. 6712–6731, 2016.
- [47] C. A. Bateson, G. P. Asner, and C. A. Wessman, “Endmember bundles: a new approach to incorporating endmember variability into spectral mixture analysis,” *IEEE Transactions on Geoscience and Remote Sensing*, vol. 38, no. 2, pp. 1083–1094, 2000.
- [48] T. Uezato, R. J. Murphy, A. Melkumyan, and A. Chlingaryan, “A novel spectral unmixing method incorporating spectral variability within endmember classes,” *IEEE Transactions on Geoscience and Remote Sensing*, vol. 54, no. 5, pp. 2812–2831, 2016.
- [49] L. Drumetz, M. Veganzones, S. Henrot, R. Phlypo, J. Chanussot, and C. Jutten, “Blind hyperspectral unmixing using an extended linear mixing model to address spectral variability,” *IEEE Transactions on Image Processing*, vol. 25, no. 8, pp. 3890–3905, 2016.
- [50] P. Thouvenin, N. Dobigeon, and J. Tourneret, “Hyperspectral unmixing with spectral variability using a perturbed linear mixing model,” *IEEE Transactions on Signal Processing*, vol. 64, no. 2, pp. 525–538, 2016.
- [51] D. Hong, N. Yokoya, J. Chanussot, and X. X. Zhu, “An augmented linear mixing model to address spectral variability for hyperspectral unmixing,” *IEEE Transactions on Image Processing*, vol. 28, no. 4, pp. 1923–1938, 2019.
- [52] A. Halimi, N. Dobigeon, and J. Tourneret, “Unsupervised unmixing of hyperspectral images accounting for endmember variability,” *IEEE Transactions on Image Processing*, vol. 24, no. 12, pp. 4904–4917, 2015.
- [53] Y. Zhou, A. Rangarajan, and P. D. Gader, “A gaussian mixture model representation of endmember variability in hyperspectral unmixing,” *IEEE Transactions on Image Processing*, vol. 27, no. 5, pp. 2242–2256, 2018.
- [54] Y. Zhou, E. B. Wetherley, and P. D. Gader, “Unmixing urban hyperspectral imagery using probability distributions to represent endmember variability,” *Remote Sensing of Environment*, vol. 246, p. 111857, 2020.
- [55] T. Uezato, M. Fauvel, and N. Dobigeon, “Hyperspectral unmixing with spectral variability using adaptive bundles and double sparsity,” *IEEE Transactions on Geoscience and Remote Sensing*, vol. 57, no. 6, pp. 3980–3992, 2019.
- [56] D. Hong and X. X. Zhu, “Sulora: Subspace unmixing with low-rank attribute embedding for hyperspectral data analysis,” *IEEE Journal of Selected Topics in Signal Processing*, vol. 12, no. 6, pp. 1351–1363, 2018.
- [57] A. Halimi, P. Honeine, and J. M. Bioucas-Dias, “Hyperspectral unmixing in presence of endmember variability, nonlinearity, or mismodeling effects,” *IEEE Transactions on Image Processing*, vol. 25, no. 10, pp. 4565–4579, 2016.
- [58] A. Halimi, J. M. Bioucas-Dias, N. Dobigeon, G. S. Buller, and S. McLaughlin, “Fast hyperspectral unmixing in presence of nonlinearity or mismodeling effects,” *IEEE Transactions on Computational Imaging*, vol. 3, no. 2, pp. 146–159, 2017.
- [59] L. Drumetz, B. Ehsandoust, J. Chanussot, B. Rivet, M. Babaie-Zadeh, and C. Jutten, “Relationships between nonlinear and space-variant linear models in hyperspectral image unmixing,” *IEEE Signal Processing Letters*, vol. 24, no. 10, pp. 1567–1571, 2017.

- [60] W. Luo, L. Gao, R. Zhang, A. Marinoni, and B. Zhang, "Bilinear normal mixing model for spectral unmixing," *IET Image Processing*, vol. 13, no. 2, pp. 344–354, 2019.
- [61] K. Siebels, K. Göita, and M. Germain, "Estimation of mineral abundance from hyperspectral data using a new supervised neighbor-band ratio unmixing approach," *IEEE Transactions on Geoscience and Remote Sensing*, vol. 58, no. 10, pp. 6754–6766, 2020.
- [62] J. F. Mustard and C. M. Pieters, "Quantitative abundance estimates from bidirectional reflectance measurements," *Journal of Geophysical Research: Solid Earth*, vol. 92, no. B4, pp. E617–E626, 1987.
- [63] R. Heylen, D. Burazerovic, and P. Scheunders, "Non-linear spectral unmixing by geodesic simplex volume maximization," *IEEE Journal of Selected Topics in Signal Processing*, vol. 5, no. 3, pp. 534–542, 2011.
- [64] B. Koirala, Z. Zahiri, and P. Scheunders, "A robust supervised method for estimating soil moisture content from spectral reflectance," *IEEE Transactions on Geoscience and Remote Sensing*, vol. 60, pp. 1–13, 2022.
- [65] B. Koirala, B. Rasti, Z. Bnoukacem, A. d. L. Ribeiro, Y. Madriz, E. Herrmann, A. Gestels, T. D. Kerf, S. Lorenz, M. Fuchs, K. Janssens, G. Steenackers, R. Gloaguen, and P. Scheunders, "A multisensor hyperspectral benchmark dataset for unmixing of intimate mixtures," *IEEE Sensors Journal*, pp. 1–1, 2023.
- [66] S. A. Trim, K. Mason, and A. Hueni, "Spectroradiometer spectral calibration, isrf shapes, and related uncertainties," *Appl. Opt.*, vol. 60, no. 18, pp. 5405–5417, Jun 2021.
- [67] R. Heylen, D. Burazerovic, and P. Scheunders, "Fully constrained least squares spectral unmixing by simplex projection," *IEEE Transactions on Geoscience and Remote Sensing*, vol. 49, no. 11, pp. 4112–4122, 2011.
- [68] J. F. Mustard and C. M. Pieters, "Photometric phase functions of common geologic minerals and applications to quantitative analysis of mineral mixture reflectance spectra," *Journal of Geophysical Research*, vol. 94, pp. 13 619–13 634, 1989.
- [69] B. Rasti, M. O. Ulfarsson, and P. Ghamisi, "Automatic hyperspectral image restoration using sparse and low-rank modeling," *IEEE Geoscience and Remote Sensing Letters*, vol. 14, no. 12, pp. 2335–2339, 2017.
- [70] M. Pharr, W. Jakob, and G. Humphreys, *Physically Based Rendering: From Theory to Implementation*, 3rd ed. San Francisco, CA, USA: Morgan Kaufmann Publishers Inc., 2016.



Bikram Koirala (Member, IEEE) received the M.S. degree in geomatics engineering from the University of Stuttgart, Stuttgart, Germany, in 2016, and the Ph.D. degree in development of advanced hyperspectral unmixing methods from the University of Antwerp, Antwerp, Belgium, in 2021.

In 2017, he joined the Vision Lab, Department of Physics, University of Antwerp, as a Ph.D. Researcher, where he is currently an FWO Postdoctoral Researcher. His research interests include machine learning and hyperspectral image processing.



Behnood Rasti (M'12–SM'19) received the B.Sc. and M.Sc. degrees in electronics and electrical engineering from Electrical Engineering Department, University of Guilan, Rasht, Iran, in 2006 and 2009, respectively, and the Ph.D. degree in electrical and computer engineering from the University of Iceland, Reykjavik, Iceland, in 2014. He was a Valedictorian as an M.Sc. Student in 2009. In 2015 and 2016, he was a Postdoctoral Researcher with Electrical and Computer Engineering Department, University of Iceland. From 2016 to 2019, he was a

Lecturer with the Center of Engineering Technology and Applied Sciences, Department of Electrical and Computer Engineering, University of Iceland. From 2022 to 2023, he was a Principal Research Associate with Helmholtz-Zentrum Dresden-Rossendorf (HZDR), Dresden, Germany. He is currently a Senior Research Scientist with Faculty of Electrical Engineering and Computer Science, Technische Universität Berlin. His research interests include signal and image processing, machine/deep learning, remote sensing, and artificial intelligence. Dr. Rasti was a Humboldt Research Fellow in 2020 and 2021. He was the recipient of the Doctoral Grant of the University of Iceland Research Fund "The Eimskip University Fund" and the "Alexander von Humboldt Research Fellowship Grant" in 2013 and 2019, respectively. He is an Associate Editor for IEEE Geoscience and Remote Sensing Letters (GRSL).



Zakaria Bnoukacem holds a M.Sc. in Surveying Engineering and Geomatics from the Agronomic and Veterinary Institute Hassan II (IAV Hassan II) in Rabat, Morocco. Currently he is enrolled as a Ph.D. researcher at the University of Antwerp's Department of Physics' VisionLab. His main research subject is material characterization using spectral reflectance for intimate mixtures.



Paul Scheunders (M'98) received the M.S. degree and the Ph.D. degree in physics, with work in the field of statistical mechanics, from the University of Antwerp, Antwerp, Belgium, in 1986 and 1990, respectively. In 1991, he became a research associate with the Vision Lab, Department of Physics, University of Antwerp, where he is currently a full professor. His current research interest includes remote sensing and hyperspectral image processing. He has published over 200 papers in international journals and proceedings in the field of image processing, pattern recognition, and remote sensing. Paul Scheunders is Deputy Editor-in-Chief of the IEEE Transactions on Geoscience and Remote Sensing and has served as a program committee member in numerous international conferences. He is a senior member of the IEEE Geoscience and Remote Sensing Society.